Received <day> <Month>, <year>; | Revised <day> <Month>, <year>; | Accepted <day> <Month>, <year>

DOI: xxx/xxxx

RESEARCH ARTICLE

Grid independence studies applied to a field-scale Computational Fluid Dynamic (CFD) Model using the Detached Eddy Simulation (DES) technique along a reach of the Colorado River in Marble Canyon

Abstract

Grid independence studies have emerged as essential methodological frameworks for comprehending the impact of domain resolution on simulating anisotropic turbulence at the river-reach scale using Large Eddy Simulation models. This study proposes a methodology to assess the loss of information in turbulent flow patterns when coarsening the computational domain, examined in a 1-km transect of the Colorado River along Marble Canyon. Seven computational domain resolutions are explored to analyze the sensitivity of turbulent flow to spatial resolution changes, utilizing the Turbulent Kinetic Energy (TKE) spectrum technique and spatiotemporal analysis of eddy structures via statistical metrics such as Root Mean Square Error (RMSE), Kullback-Leibler (KL) divergence, Nash-Sutcliffe Model Efficiency Coefficient (NSE), wavelet power spectrum, and Grid Convergence Index (GCI). Based on physical principles and statistics, these metrics quantify information loss and assess domain resolutions. A Computational Fluid Dynamic (CFD) model is developed by employing the Detached Eddy Simulation (DES) technique, with Boundary Condition (BC) integrating the rough wall extension of the Spallart-Allmaras model in cells near the bed. Evaluation of domain resolutions aims to identify grid cell sizes capturing flow behavior and hydraulic characteristics, including primary and secondary flows, return currents, shear layers, and primary and secondary eddies. The study observes an increase in data representation of the TKE spectrum with finer spatial domain resolution. Additionally, surface analysis, conducted via RMSE, KL, and NSE metrics, identifies specific areas within the flow field showing high sensitivity to refining the grid cell sizes.

KEYWORDS:

Colorado River, Computational Fluid Dynamics, Fluvial Geomorphology, Detached Eddy Simulation

1 INTRODUCTION

Computational Fluid Dynamic (CFD) models commonly used in river systems are statistically parameterized, such as Reynolds Averaged Navier-Stokes (RANS) models and Unsteady RANS (URANS), or eddy-resolving models, such as the Large Eddy Simulation (LES) and Detached Eddy Simulation (DES) (Ferziger and Peric 2002). In RANS and URANS techniques, Reynolds stress tensors are modeled using the Boussinesq approximation, which assumes that turbulence is isotropic (Durbin and Reif 2011; Pope 2000). Therefore, in RANS and URANS techniques, turbulence scales are modeled by isotropic eddy viscosity (Durbin and Reif 2011; Nagata et al. 2005; Nikora et al. 2007; Sinha et al. 1998; Pope 2000), except for Reynolds Stress Modeling (RSM) where anisotropic turbulence from Reynold's stress tensor is simulated directly by solving a transport equation for each stress component (Safarzadeh and Brevis 2016). As supercomputer capabilities advance, current turbulence-resolving models can be implemented on a large scale to understand fluid dynamics in rivers when treated as learning environments (Alvarez et al. 2017; Alvarez and Grams 2021; Khosronejad et al. 2023). Eddy-resolving models can be used to quantify anisotropic turbulence by solving the Navier-Stokes equations using Large Eddy Simulation (LES), Direct Numerical Simulation (DNS), and Detached Eddy Simulation (DES) techniques. DNS cannot be applied at the river reach scale due to its significant computational expenses (Almohammadi et al. 2013; Kuwata and Kawaguchi 2019; Onofre R. and Mura 2022). Currently, DNS techniques are mainly limited to studying anisotropic turbulence at laboratory scales (Im et al. 2004; Noto 2009; Özyilmaz et al. 2008; Zhao and Xu 2023; Zaynetdinov et al. 2023). In contrast, DES techniques can be applied to the river-reach scale by implementing sub-grid scale (SGS) models. In these techniques, turbulence above the grid scale is directly resolved by the filtered Navier-Stokes equations, while eddies smaller than the grid scales are modeled. DES techniques offer computational savings compared to LES because it combines RANS near grid bed cells and LES away from boundary conditions (Aupoix and Spalart 2003; Ferziger 1985; Grinstein et al. 2007; Squires 2004a; Squires 2004b; Alexandrov et al. 2022; Bhushan et al. 2022).

Grid independence studies have become relevant tools for understanding the effect of domain resolution in a simulation of anisotropic turbulence at the river reach scale while using LES or DES models. The studies conducted by Roache (1994), Roache (1997), Roache (1998), and Lee et al. (2020) and Samion et al. (2019) proposed a theoretical framework to quantify and numerically analyze errors of different grid sizes using the Grid Convergence Index (GCI). However, Roache (1998) GCI method requires a more complex calculation than the conventional grid independence test (Lee et al. 2020). Eça and Hoekstra (2014) established a procedure to estimate the numerical uncertainty of any integral or local flow quantity resulting from fluid flow simulations based on grid refinement studies. Later, Samion et al. (2019) implemented a grid convergence study for the DES of flow over the rod-airfoil configuration using the Computational Fluid Dynamic Solver: OpenFOAM (Open Field Operation And Manipulation) (Chen et al. 2014). More recently, Piasecka et al. (2022) and Van Hoecke et al. (2023) performed a mesh dependency analysis using the GCI method recommended by the Fluid Engineering Division of the American Society of Mechanical Engineers (ASME) based on the Richardson extrapolation principle. This research aims to study the loss of data representation of macro-turbulence under a set of spatial domain resolutions (Lee et al. 2020). Thus, a grid convergence study allows the evaluation of resolved anisotropic turbulence and eddy structures based on the filtered governing continuity and momentum equations under the DES implementation. The relative error gap versus the experimental data between the coarse and fine meshes shows the sensitivity of the DES results to grid refinement (Huck et al. 2019; Squires 2004a). Previous grid independence studies have shown an improvement in the performance of parallelized eddy-resolving models by optimizing the spatial domain resolution and saving computational expenses (Baker et al. 2020a; Seifollahi Moghadam et al. 2021; Xiao et al. 2017). Therefore, resolved quantities such as velocity and pressure could be sensitive to resolution and mesh characteristics.

When tested on the scale of fluvial systems, eddy-resolving models could benefit from a methodological study that clarifies how turbulence is represented and how information is lost when grid cells are coarsened within the computational domain. The loss of information can be interpreted in terms of spatial detail; fine mesh resolutions capture smaller-scale features and variations in the data. As the resolution becomes coarser, these fine details are no longer represented, leading to a loss of spatial detail. In addition, there is yet to be a definitive method framework to guide the construction of an accurate computational mesh to develop field-scale turbulence models for river systems. Furthermore, the appropriate resolution of a simulation depends on both the model's purpose and the accuracy requirements. Therefore, independent studies are needed on turbulence-resolving models applied to fluvial systems at both the field and the laboratory scales and establish a research framework to evaluate data representation in multiple computational domains (Lee et al. 2020; Roache 1997; Roache 1998; Roache 1994; Samion et al. 2019). The proposed study aims to fill the gaps in the literature, particularly the topic of grid convergence studies and their role in simulating turbulent flow in river systems at the field scale.

Two primary questions are addressed. First, how are large-scale hydro-morphodynamic patterns, including primary and secondary flows and shear layers, simulated under different domain resolutions? The sensitivity of field-scale models to the spatial resolution of the computational domain is calculated to identify complex turbulent flow patterns in river systems. Second, how can the loss of information from a benchmark LES model be quantified as a result of implementing coarser grids? The model representation of turbulent flow is evaluated using physical and statistical techniques to quantify information gain or loss across a set of domain resolutions. The grid independence analysis is applied to an eddy-resolving model at the river-reach scale, along a transect of the Colorado River in Marble Canyon, Arizona. A river transect is denoted as a specific reach of the river. The river transect under analysis is the Eminence Break (EM) fan eddy complex, located at Kilometer 97 of the Colorado River from 108 Lees Ferry in Marble Canyon. The methodological framework used seven different computational domain resolutions to analyze the sensitivity of field-scale models to spatial resolution changes employing various techniques such as the turbulent kinetic energy spectrum, spatiotemporal analysis of eddy structures, Kullback–Leibler (KL) divergence, Nash–Sutcliffe model efficiency coefficient (NSE), wavelet power spectrum, and GCI calculation. A statistical method based on the Root Mean Square Error (RMSE) metric was used to assess the accuracy of the model's representation of flow behavior, hydraulic characteristics, primary and secondary flows, shear layers, and primary and secondary eddies. A frequency spectrum analysis was performed to evaluate the ability of the different grid resolutions to capture eddy pulsations of various scales by analyzing the energy spectrum of turbulence in the frequency domain and the time series of velocity fluctuations (Navah et al. 2020; Wang et al. 2023; Al-Jumaili and Mulahasan 2023). The KL - divergence function was used to quantify the information loss between the prior and posterior probability model distributions for all domain resolutions (Patel et al. 2023; D'Ortenzio et al. 2022; Smith et al. 2006). NSE was used as a goodness-of-fit index (E_f) to evaluate the accuracy of the results obtained for each grid resolution compared to the benchmark case scenario. Wavelet analysis was performed to assess the ability of the six computational domain resolutions to capture eddy pulsations at spatial-temporal scales relative to the benchmark case scenario (Fiedler 1988; Chen et al. 2019). The wavelet time-frequency analysis helped identify fluctuations that produce kinetic energy at larger scales and captured localized processes at smaller scales that contain high-energy events in time series. Finally, GCI calculation was utilized to estimate the numerical error due to discretization and determine the necessary grid resolution for achieving the desired level of accuracy (Roache 1998; Phillips and Roy 2014; Baker et al. 2020b).

2 STUDY AREA

Canyon-bound rivers with debris fan constrictions are conducive to rapids and pools and are characterized by large eddy-flow structures due to the morphology of the channel (Garrett et al. 1993; Grams 1997; Howard and Dolan 1981). Fine sediment deposition and erosion occur in areas closely related to secondary flow structures within a fan eddy complex (Figure 1). Schmidt and Rubin (1995) described the fan-eddy complex as a combination of geomorphic elements, including a debris fan and a rapid, along with a lateral separation zone where primary and secondary eddies recirculate. The fan-eddy complex also includes a downstream gravel bar consisting of coarse material derived from the reworked debris fan. Other notable features of the fan-eddy complex include channel constriction, channel expansion, and a deep pool downstream of the constriction (Garrett et al. 1993; Grams 1997; Howard and Dolan 1981; Leopold 1969; Schmidt 1990; Schmidt et al. 1999; Wright and Kaplinski 2011). The study area is essential for its ecological, biological, tourist and economic value (Converse et al. 1998; Draut and Rubin 2008; Alvarez and Schmeeckle 2013; Hartwell 2020). For example, the lower part of the Colorado River basin provides water to the states of California, Arizona, and Nevada and produces hydroelectric power (Harpman 1999; Melis et al. 2015; Schmidt et al. 1999; Webb et al. 1999). Lateral separation eddy bars have been important for environmental and recreational resources, the protection of archeological sites, and tourist purposes. Eddy bars play a role in the habitat for endangered fish species (Converse et al. 1998; Dodrill et al. 2015; Gerig et al. 2014; Korman et al. 2004; Turner et al. 2016); Therefore, an accurate representation and prediction of the flow and sediment patterns would help to manage this ecosystem.

The DES model proposed in this study was used to simulate the geomorphologic features of the fan eddy complex in the main channel and the lateral separation zone downstream of the rapids, which extends from the separation point to the reattachment points. The focus is on primary and secondary flows, return currents, and other complex features, such as shear layers, that occur when there is a significant velocity gradient in the transition from the lateral recirculation zone to the main channel. The research is conducted at the Eminence Break (EM) fan eddy complex, located on kilometer 97 of the Colorado River from Lees Ferry in Marble Canyon (Figure 1). Massive flow separation, strong secondary flows, and complex sediment transfer dynamics from the main channel characterize the lateral separation zone in this area.

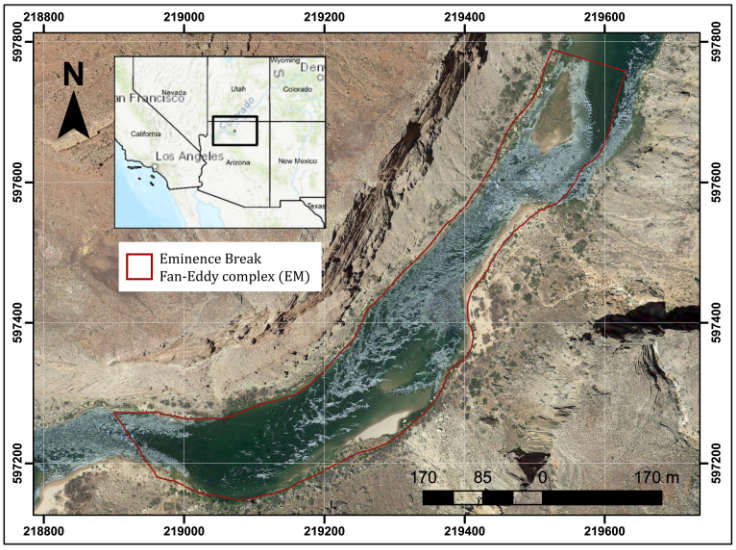

FIGURE 1 Map of the study area, Eminence Break (EM) fan-eddy complex, situated at the 97th-km mark along Marble Canyon of the Colorado River, starting from Lees Ferry.

The Colorado River descends approximately 670 meters in elevation over a distance of 450,616 meters through the Grand Canyon, resulting in an average river slope of approximately 0.0015 (Leopold 1969). The modeled river reach extends about 1 km in length, with widths ranging from 78 m to 149 m and depths varying between 0.6 m and 17 m, and energy slope was calculated to be equal to 0.00282. Table 1 provides a statistical summary of the width and depth within the computational domain. The median grain size D_{50} of the riverbed was determined from field measurements, with a representative value of 0.05 m selected to characterize the riverbed composition within the modeled reach. This value corresponds to the grain composition, typical of the main channel. However, due to the natural variability in grain size, using a single D_{50} value of 0.05 m for this study reach is a simplification (Buscombe et al. 2014). While the main channel exhibits grain sizes in this range, other sections, such as lateral recirculation zones, may contain significantly finer sediments. In the OpenFOAM model, the roughness height K_s was prescribed as a constant value. Applying the relationship K_s equal to $2D_{50}$ (Garcia 2008) resulted in a roughness height of 0.10 m, implemented using OpenFOAM's nutURoughWallFunction boundary condition. This approach ensured that the model simulated the roughness imposed by the riverbed material, maintaining consistency between measured grain composition characteristics and computational roughness parameters.

3 METHODOLOGY

This study used the parallelized, three-dimensional eddy-resolving model developed by Alvarez (2015), Alvarez et al. (2017), and Alvarez and Grams (2021) as the benchmark case to analyze the model sensitivity to grid scales and to identify complex turbulent structures of the canyon-bound rivers. Thus, the DES model was validated at the Re_5 resolution according to previous results published in Alvarez et al. (2017). The dataset used to validate such DES model (including its selected domain resolution) consisted of Acoustic Doppler Current Profiler (ADCP) data collected during the 2008 controlled flood release from Glen Canyon Dam, with velocity profiles measured at 4920 sites across ten transects within the EM and WT fan-eddy complexes. These data were used to build the computational domain, define initial and boundary conditions, and validate three-dimensional flow structures. The model's predictive capabilities were assessed through point-to-point comparisons of time-averaged simulated and observed velocities, using metrics such as Mean Absolute Error (MAE), Root Mean Square Error (RMSE), and Pearson Correlation Coefficient (R). The model accurately predicted the flow characteristics, including eddy size, position, and return currents, with an MAE of 0.296 m/s, an RMSE of 0.4 m/s, and a Pearson correlation of 0.874. Despite errors in complex regions, such as lateral separation zones, the DES-3D model outperformed two-dimensional models, accurately capturing turbulence and short-term eddy pulsations critical for understanding turbulence and sediment transport (Alvarez et al. 2017).

The benchmark scenario employed the DES technique with a spatial resolution of 5,625,000 cells. The simulation required 24 hours of processing time on 128 processors to simulate 15 min at a time step of 0.1 s. The accuracy of the model was evaluated through point-to-point verification by comparing its ability to reproduce Acoustic Doppler Current Profiler (ADCP)

TABLE 1 The depth and width statistics of the computational domain, adopted from Alvarez and Grams (2021), are presented.

Statistics	Min	1st Quartile	Median	Mean	3rd Quartile	Max
$Depth(m)$	0.6	3.8	6.0	6.3	8.2	17.0
$Width(m)$	78.5	111.4	124.6	121.0	135.0	149.0

flow measurements obtained during a controlled flood. The validation process and statistical metric values of the eddy-resolving used as a benchmark case in this study can be found in Alvarez et al. (2017). The developed solver and data are publicly available and have been published in Grams et al. (2021). The validation process involved the use of six statistical metrics to quantify spatially distributed velocity field errors against field observations to evaluate grid resolution and model forecasting capabilities. The skill metrics used for evaluation included four absolute error scores: Mean Absolute Error (MAE), Mean Forecast Error (MFE), RMSE, and Pearson correlation coefficient (R), as well as two relative error metrics: Mean Absolute Percentage Error (MAPE) and Median Absolute Percentage Error (MdAPE). The statistical scores used to evaluate the model indicated relatively small error values for all six metrics. Additionally, the similarity between the cumulative and probability density functions of observed and simulated data suggested a good fit between the observed and simulated density functions (Alvarez et al. 2017).

3.1 Numerical Methods and Governing Equations

This model employed the DES technique under its decomposition, where variable fields greater than the spatial filter are termed filtered variables and are represented with an overline. Components smaller than the spatial filter are termed sub-grid scale variables and are represented by a prime. The continuity (equation 1) and Navier-Stokes (equation 2) equations are the governing equations for the flow field. These equations are shown below in terms of the LES decomposition:

Continuity:

$$\frac{\partial \bar{u}_i}{\partial x_i} = 0 \tag{1}$$

Momentum:

$$\frac{\partial \bar{u}_i}{\partial t} + \frac{\partial \bar{u}_i \bar{u}_j}{\partial x_j} = -\frac{1}{\rho}\frac{\partial \bar{p}}{\partial x_i} + \frac{\partial}{\partial x_j}\left((\nu\prime + \nu\prime_t)\frac{\partial \bar{u}_i}{\partial x_j}\right) \tag{2}$$

Where $\bar{u}$ and p are the filtered velocity and pressure components, ρ is the density, ν is the molecular viscosity, and the ν_t is the eddy viscosity. The term containing the molecular viscosity and eddy viscosity is $(\nu\prime + \nu\prime_t)$ and represents the unresolved subgrid (SGS) stress tensor, and it is modeled using the Spallart Allmaras (S-A) turbulence closure. This model was chosen because it is a non-zonal technique; therefore, prior declaration of RANS zones versus LES zones is not necessary (Squires 2004a). The length scale $\bar{d}$ of the S-A model is equal to the minimum of the distance to the bed or banks, d, and the length scale, proportional to the local grid spacing, $C_{DES}\Delta_G$. The term C_{DES} is the adjustable model constant, the value of C_{DES} varies with mesh size because it is related to the representation of turbulence features in the flow. In this analysis the empirical constant C_{DES} is represented as the ratio between the benchmark case and the generated grid resolutions Re_0. The lower values of C_{DES} were assigned to finer mesh resolutions to account for the increased spatial detail captured by the grid. Δ is based on the largest dimension of the local grid cell between $\Delta = max(\delta_x, \delta_y, \delta_z)$ and $\bar{d} = min(d, C_{DES}\Delta_G)$. The CDES value of 0.65 was employed in the DES model, as commonly recommended in the DES literature (Spalart et al. 1997; Spalart 2009; Shur et al. 1999; Travin et al. 2000). This value is computed internally by the OpenFOAM code and ensures consistency with established DES methodologies.

The Pressure Implicit with Splitting of Operators (PISO) algorithm was used as a computational method to solve the Navier-Stokes equations. This iterative algorithm enhances the accuracy of pressure and velocity coupling through a predictor-corrector approach, ensuring the satisfaction of both the momentum and continuity equations. By iteratively refining the pressure and velocity fields, PISO effectively handles the nonlinearity of the governing equations and achieves faster convergence compared to other methods, making it particularly efficient for this DES model.

3.2 Boundary conditions and initial conditions

The boundary condition (BC) at the bed is non-slip and integrates the rough wall extension of the S-A model (Aupoix and Spalart 2003) in the cells near the bed. For solid boundaries, Ligrani and Moffat (1986) from the log-law equation is employed, where z_0 equals $0.033k_s$. This formulation is based on experimental data from Nikuradse (Garcia 2008). The rough wall function (nutRoughWallFunction) is built into the OpenFOAM environment and uses the velocity in the first grid cell near the bed to calculate the turbulent viscosity $\nu\prime_t$ at the wall. The roughness height (k_s) was required as input to most of the $\nu\prime_t$ wall equations to ensure a layer of rough wall logs between the center of the first grid cell near the bed and the wall. The first grid cell closest to the bed was 5 cm, k_s was estimated to be 10 cm, and therefore z_0 was equal to 0.3 cm. The BC roughness in the bed and the BC roughness at the entrance resulted in flow structures that propagated throughout the domain and established fully developed turbulence. The boundary condition at the water surface was specified as free slip, while a rough wall condition was imposed along the lateral boundaries. The Initial Condition (IC) for the flow at the input of the numerical model was set to coincide with the constant maximum discharge of the 2008 controlled flood, equal to $1189 m^3/s$.

The "mapped" boundaryField condition from the OpenFOAM environment was used to specify the boundary conditions for the inlet boundary based on mapped values from the benchmark case mesh and ensure a fully developed turbulent flow. The "mapped" boundary condition reads the mapping files at each time step and interpolates the flow properties from the benchmark case mesh to the specified inlet boundary of the generated mesh. These interpolated values were used as the inlet boundary condition to simulate the generated computational domains. The "cell" interpolation scheme was used, which utilizes cell-based interpolation to transfer the flow properties accurately.

The selected boundary distance of 160 meters ensures a fully developed turbulent state upstream of the lateral separation zones, which are the focus of this study. This distance was determined based on several key factors. Primarily, large-scale turbulent eddies typically scale with flow depth; thus, setting the mapped boundary at 10 times the maximum depth allows for adequate resolution of macroturbulence before it enters the computational domain. The largest turbulent eddies are captured using the maximum depth of the simulated river reach—a crucial aspect for this study, given its focus on complex flow features such as primary and secondary eddies, return channels, and free shear layers. Furthermore, this distance stabilizes the inflow profile, minimizing the risk of numerical instabilities. A smaller boundary depth would risk under-resolving these large-scale eddies, reducing simulation accuracy. Overall, the selected range balances resolving turbulence and maintaining computational efficiency. Simulation results demonstrated that this chosen value enhances accuracy by enabling large eddies to resolve within the grid effectively.

3.3 Computational Domain

A two-dimensional depth-averaged model was developed to determine the water surface elevation, subsequently used to construct the computational domain at the water level (Grams et al. 2021). The computational domain was constructed using a structured grid of hexahedral cells (Figure 2). The Finite Volume Method (FVM) discretized the computational domain into control volumes and applied conservation laws to solve the Navier-Stokes equations, ensuring accurate flux calculations across volume boundaries. Six computational domains were developed (Table 2), and the grid was partitioned into subdomains by domain decomposition, with each subdomain assigned to 128 processors. Communication between processors at the High-Performance Computing (HPC) facility of the University of Texas at El Paso was facilitated through Open MPI (Message Passing Interface). The scalability of the model, previously evaluated by Alvarez et al. (2017), was found to be stable up to 128 processors. The processing time for the model run ranged from approximately 28 to a maximum of 85 hours for a simulated time of 33 min, with a time step of 0.1 seconds. In Table 2 , R_e represents the ratio between the benchmark case and the generated grid resolutions. To ensure stability at each time step and mesh resolution, the Courant-Friedrichs-Lewy (CFL) condition (Courant et al. 1928) was maintained at ≤ 1.0.

In Figure 3 , a comparison is presented between three different mesh resolutions: the coarser mesh (Re_0), the medium size mesh (Re_3), and the fine mesh obtained from the benchmark case. The refinement of these meshes is depicted in Table 2 , which highlights that the refinement occurred in the X and Y directions while keeping the Z direction constant. The Z-resolution in the computational domain varies with river depth, as the total number of cells remains constant at 25. The only fixed cell is the first near-bed grid cell, which is set to 5 cm. The finest grid resolution, consisting of 7.2 million elements, was refined only in the Y direction. If the grid resolution Re_0 is 99 times coarser than the mesh size of the benchmark case Re_5, it means

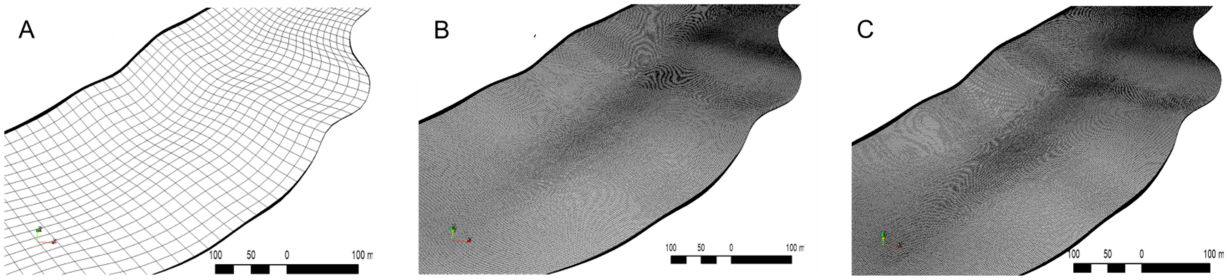

FIGURE 2 Computational domains at different grid resolutions. A) Coarser grid resolution (Re_0). B) Finest grid resolution (Re_6). C) Benchmark case (Re_5).

TABLE 2 Domain resolution specifications

Name	Number of cells	Total # of elements	(Cell Size Re) ÷(Cell Size Re_5)	Representative volume (m^3)	Total core-hours
Re_0	119 x 19 x 25	56525	99.5	38.08	28.4
Re_1	450 x 120 x 25	1350000	4.2	1.71	50
Re_2	650 x 130 x 25	2112500	2.7	0.95	56
Re_3	850 x 140 x 25	2975000	2	0.75	63.16
Re_4	950 x 150 x 25	3562500	1.6	0.64	66.75
Re_5 (BC)	1500 x 150 x 25	5625000	1	0.39	82.1
Re_6	1150 x 250 x 25	7187500	0.78	0.33	85.6

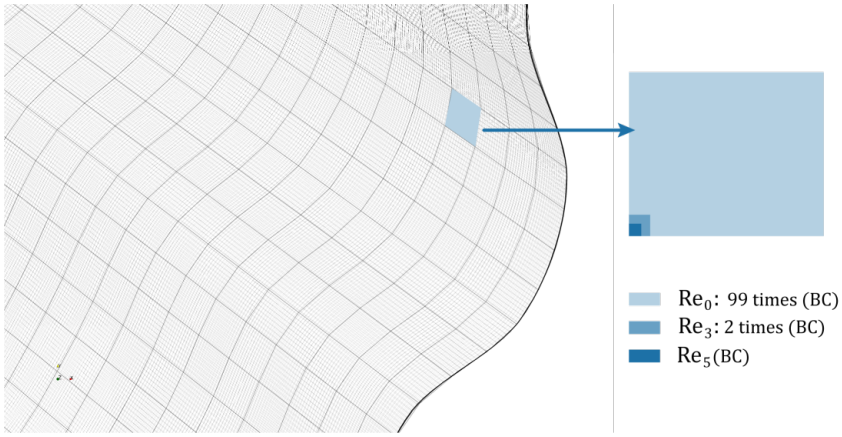

FIGURE 3 Representation of the cell size at different resolutions. The Coarser grid resolution, (Re_0), is 99 times coarser than the benchmark case domain resolution. The grid resolution (Re_3), represented in blue, is two times coarser than the benchmark case.

that within a single cell of Re_0, it is possible to fit 99 cells of Re_5. In other words, the cell size of Re_0 is significantly larger compared to the cell size of Re_5, allowing a much greater number of smaller cells to fit within it.

The resolution of the bathymetry at the riverbed is approximately 1 m x 1 m in the horizontal (x-y) plane. The bathymetry was derived from a digital elevation model (DEM) created using field-measured bathymetric data, which served as the boundary condition at the bed for the DES model. The horizontal coordinates are based on the North American Datum of 1983 (NAD83), Arizona State Plane Central Zone, while elevations are ellipsoid heights referenced to the Geodetic Reference System 1980

(GRS 80) ellipsoid defined by NAD83.

This bathymetic data was used to render the Delaunay 3D triangulation employed to construct the computational domain at the bed. The computational grid was generated using a mass-conservative mesh generation solver, that was coded and implemented in the OpenFOAM environment. This code, publicly available through Grams et al. (2021), enables the vertical axis (z) to adapt to bed elevation, while the horizontal axes (x and y) remain constant. A one-parameter hyperbolic tangent stretching function was applied along the z-axis to calculate the vertical resolution of the grid. The grid spacing was designed to refine near-bed cells while gradually increasing resolution toward the surface water level.

4 RESULTS

4.1 Velocity and vorticity patterns

The study was conducted using seven resolutions in the computational domain. The spatial computational domain resolutions included six generated simulations (Re_0, Re_1, Re_2, Re_3, Re_4, and Re_6) and the benchmark case (Re_5), as listed in Table 2 . This subsection aims to evaluate the sensitivity of field-scale generated computational models to the spatial resolution of the computational domain to identify complex turbulent flow patterns in the hydraulic features present in the Colorado River in Marble Canyon, Arizona. Domain resolutions Re_0 (lowest resolution), Re_3 (medium resolution), Re_5 (Benchmark case), and the finest resolution Re_6 were analyzed. Several simulation videos (Appendix D) and figures were produced to better illustrate the findings, mainly focusing on velocity vector structures (Figure 4 and Movie 1), velocity field (Figure 5 and Movie 2), Q-criterion (Figure 6 and Movie 3), and vorticity (Figure 7 and Movie 4).

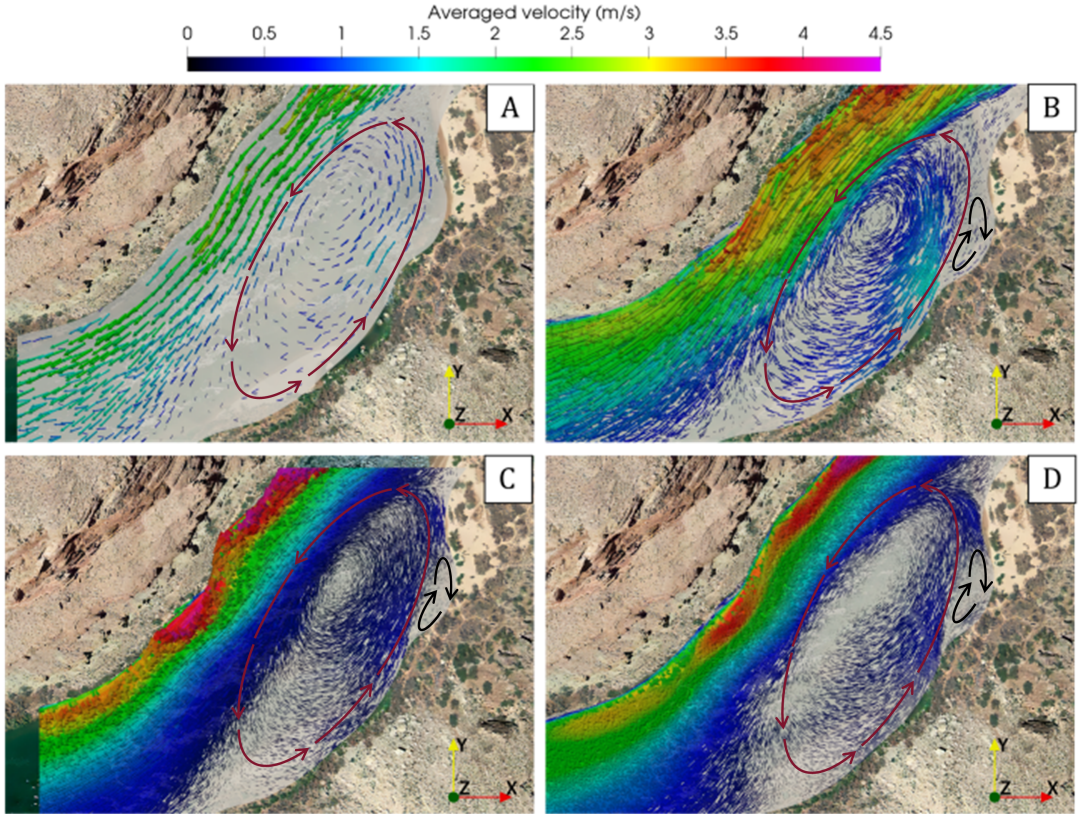

FIGURE 4 Simulated velocity vectors at near-surface grid cells for the domain resolutions. A) Lowest resolution (Re_0). B) Medium resolution (Re_3). C) Finest resolution (Re_6). And D) Benchmark case (Re_5), based on the simulated averaged velocity (m/s). The red and black arrows indicate the primary and secondary eddy,s respectively

The purpose of analyzing velocity vectors is to assess how well the generated domain resolutions can reproduce short-term temporal changes in velocity vector directions, anisotropic turbulence with massive flow separation away from solid boundaries, and the presence of eddy pulsations. According to Figure 4 and Movie 1, a secondary eddy in a clockwise direction formed

near the separation zone on the left side of the riverbank. The computational resolution Re_0 (Figure 4 A) could not reproduce the formation of the secondary eddy structure and the return current. Instead, it depicted a significantly large primary eddy structure with a weak return current with velocities between 1 and 1.5m/s. In resolution Re_3 (Figure 4 B), the velocity vectors showed a well-defined primary eddy and a return current with velocities between 1 and 1.5 m/s similar to those observed in Re_5 and Re_6, resolution Re_3 also captured the formation of the secondary eddy. The models with resolutions Re_6 (Figure 4 C) and Re_5 (Figure 4 D) displayed a large primary eddy with a strong return channel and a relatively smaller secondary eddy. Additionally, increased temporal variability in the velocity direction was observed in the EM transect within the separation and reattachment zones. The findings of this analysis indicated that the resolutions of the medium to finer domain, starting at Re_3, can simulate the main recirculation zones along the lateral recirculation zone. Specifically, the resolution Re_3 accurately captured the main patterns of the velocity vectors for the primary and secondary eddies and the return current.

The velocity field simulated for the domain resolutions Re_0, Re_3, Re_5, and Re_6 is shown in Figure 5 and Movie 2. On the left bank, the velocity values are higher compared to the lateral separation zone. Furthermore, the minimum velocity values are found in the lateral recirculation zone in the separation and reattachment zones. Re_0 (Figure 5 A) did not accurately reproduce these patterns compared to the results of the benchmark case scenario, while the resolutions Re_3, Re_5, and Re_6 (Figures 5 B, C, and D, respectively) successfully captured these turbulent flow patterns. The results obtained from simulations at resolutions Re_3, Re_4, and Re_5 successfully captured the deceleration of flow at the expansion as it transitions from rapid to pool (see Figures 5 B, C, and D). Hence, the velocity field along the main channel during this transition was well captured compared to the benchmark case. In contrast, the resolution Re_0 failed to reproduce this process, as velocities ranging from 1.5 to 2 m/s were observed along the main channel during the transition to the pool, which is significantly lower compared to the velocities observed in the benchmark case scenario Re_5, ranging from 2.5 to 3.7 m/s, as shown in Figures 5 A and D.

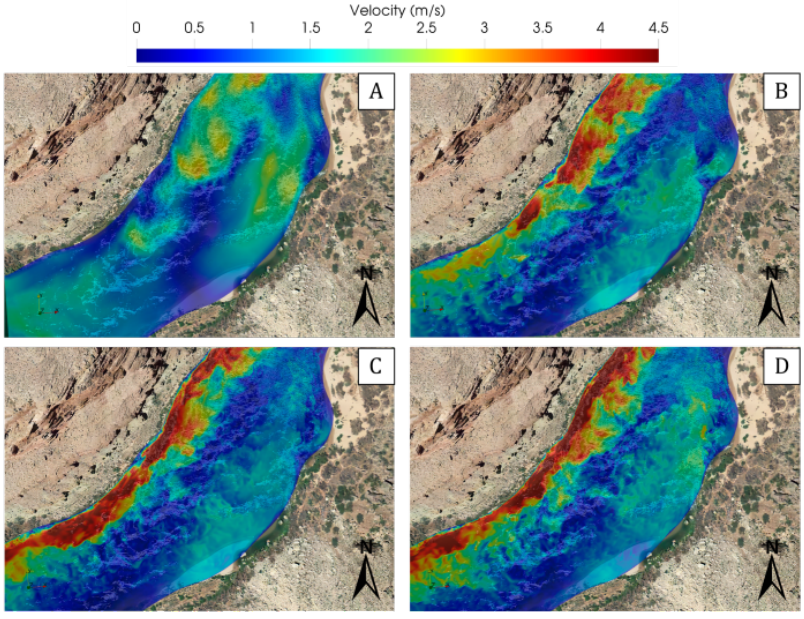

FIGURE 5 Simulated velocity field at near-surface grid cells for the domain resolutions. A) Lowest resolution (Re_0). B) Medium resolution (Re_3). C) Finest resolution (Re_6). And D) Benchmark case (Re_5), based on the simulated averaged velocity (m/s).

Figure 6 and Movie 3 showed a two-dimensional plan of a transient turbulent structure identified by the iso-surfaces of the Q-criterion, equal to 1 cm, are colored by velocity magnitude for domain resolutions Re_0, Re_3, Re_5, and Re_6 at the near-bed grid cells. The results indicated that resolution Re_0 (Figure 6 A) provided a coarse representation of the Q-criterion iso-surfaces and could not capture the shape and magnitude of the velocity field of the turbulence structures. The resolutions Re_3 and Re_6 (6 B and C) showed transient vortical structures formed along the main channel and in the secondary eddy zone; these patterns were also identified in the benchmark case scenario. Resolutions Re_3 and Re_6 successfully captured the Q-criterion iso-surfaces generating similar results to the ones obtained for Re_5 (Figure 6 D).

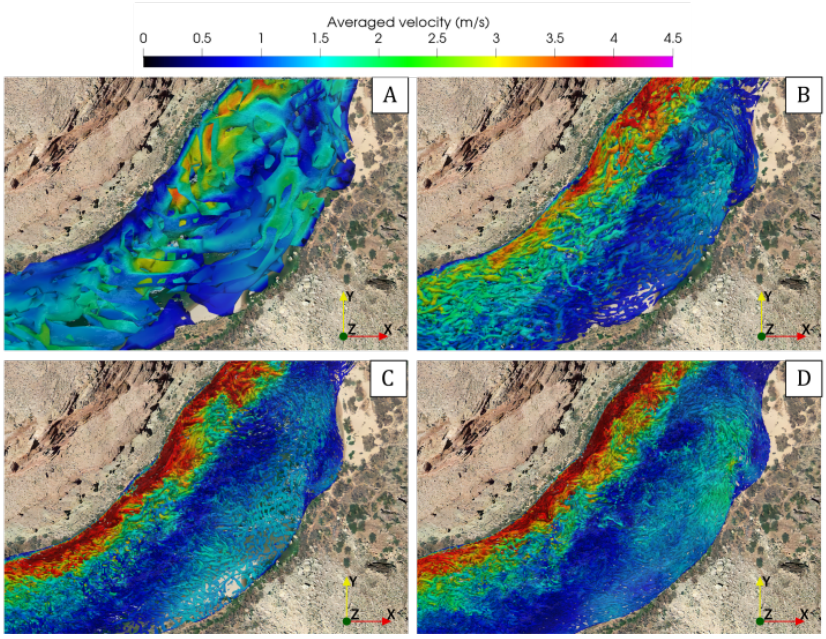

FIGURE 6 Iso-surfaces of Q-criterion colored by velocity magnitude for the domain resolutions. A) Lowest resolution (Re_0). B) Medium resolution (Re_3). C) Finest resolution (Re_6). And D) Benchmark case (Re_5).

The vertical component of vorticity for domain resolutions Re_0, Re_3, Re_5, and Re_6 at the near-bed grid cells is shown in Figure 7 and Movie 4. The vorticity patterns for turbulence structures in the vertical component are illustrated in Figure 7 . Figures 7 B, C, and D showed the presence of large-scale turbulence structures with positive vorticity values along the main channel and the return current, which exhibited counterclockwise rotation. However, the turbulence structures in the secondary eddy and the separation zone, which rotate in a clockwise direction, showed negative vorticity values. The highest vorticity values were observed along the main channel and the secondary eddy zone.

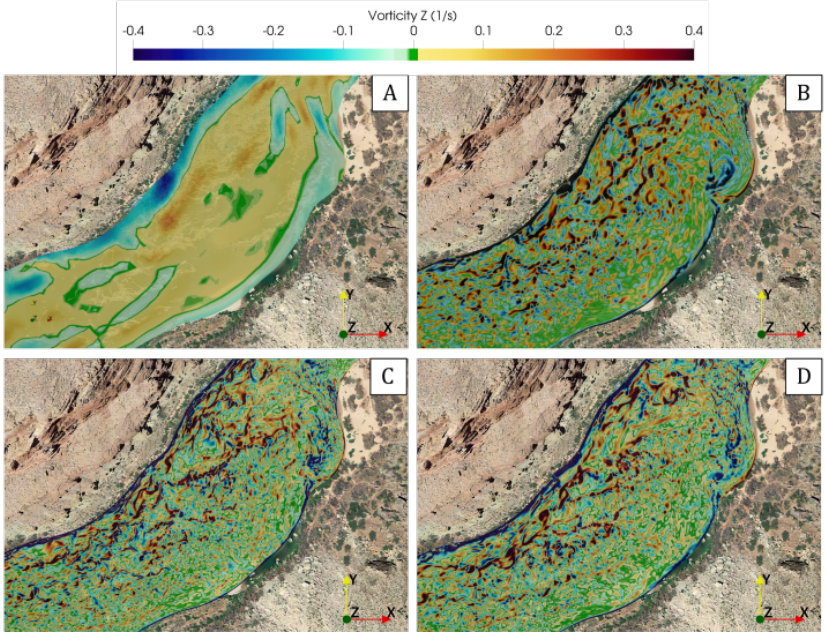

FIGURE 7 Vertical component of vorticity for the domain resolutions. A) Lowest resolution (Re_0). B) Medium resolution (Re_3). C) Finest resolution (Re_6). And D) Benchmark case (Re_5).

The results indicated that the domain resolutions Re_3 and Re_6 successfully captured the magnitude and direction of large-scale turbulent structures, with vorticity predominantly in the vertical direction compared to the benchmark case scenario Re_5,

showing no sensitivity to the refinement of the computational domain beyond the resolution Re_3 which is twice as coarse as the benchmark case Re_5.

4.2 Time series analysis

4.2.1 Energy spectrum

This analysis was developed through the turbulence energy spectrum in the frequency domain (readers are referred to Appendix A1, Figure A1 for an explanation of the energy spectrum) and a time series of velocity fluctuations at eight representative points located at separation, reattachment zones, primary and secondary eddy in the lateral separation zone of the fan-eddy complex (see Figure 8). This analysis helped to identify fluctuations that produced kinetic energy at larger scales and captured localized processes at smaller scales that contained high-energy events in the time series. The location of the point probes for this analysis is primarily at two and at six-tenths of the channel depth, which represents the near-surface grid cells and the average velocity of the velocity profile, respectively. Figure 8 A shows the EM transect, which serves as the main focus of this analysis, and Figure 8 B shows the specific site locations of the point probes. The energy spectrum of turbulence was obtained by performing a Fast Fourier Transform (FFT) on the velocity data.

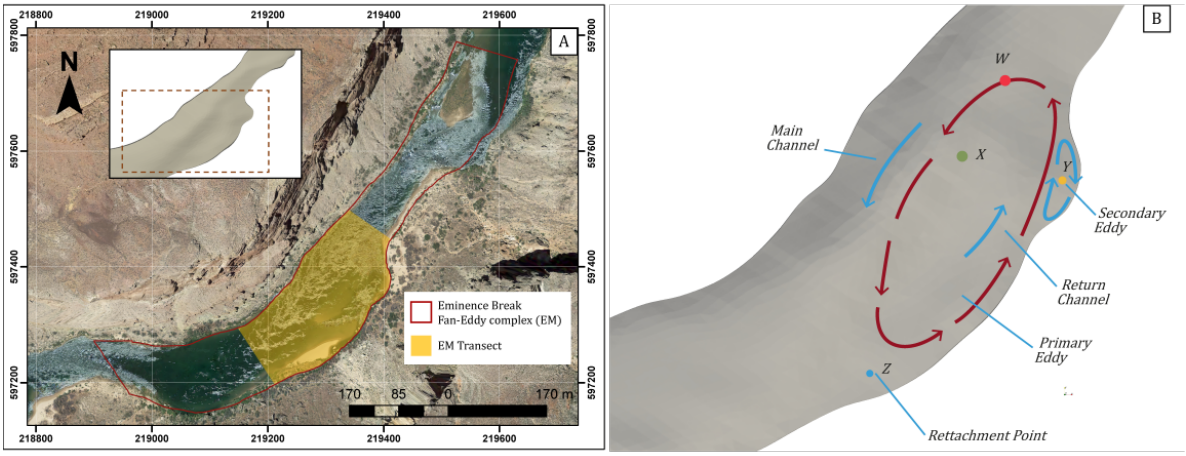

FIGURE 8 (A) Map showing the location of EM transect (in yellow), the primary area of interest for this analysis. (B) Point probes in sites W, Z, X, and Y are located at separation, reattachment zones, and primary and secondary eddies. The point probes are located 1) at two-tenths of the total depth (near-surface grid cells) with coordinates $P(x, y, z)$: P_w(219362, 597443, 841.11), P_z(219218, 597232, 839.18), P_x(219356, 597397, 838.951) and P_y(219384, 597373, 839.812) and 2) at six-tenths of the channel depth grid cells (average velocity for the velocity profile) with coordinates: P_w(219361, 597445, 835.782), P_z(219210, 597227, 838.77), P_x(219354, 597401, 835.677) and P_y(219384, 597374, 837.823).

The energy distribution in the frequency domain within the inertial scaling regime was characterized by Kolmogorov's postulated negative 5/3 power law. In other words, the main contribution to the total velocity variance and energy motion comes from the low frequencies. Thus, the dominant frequencies of turbulence range from 0.002 to 0.04 Hz in the separation zone and secondary eddy (see Figures 9 A and B, and 10 A and B) and from 0.002 to 0.01 Hz in the reattachment zone and primary eddy (see Figures 9 C and d, Figures 10 C and D), with a rapid energy decrease as frequency increases. Most of the energy peak occurs at frequencies ranging from 0.002 to 0.05 Hz. This suggested a predominant pattern of eddy pulsations in the separation and reattachment zones at six-tenths of the channel depth grid cells, as shown in Figures 9 and Figure 10 . It was observed that in the six simulated computational domain resolutions, the flow fluctuations at the separation zone and the primary eddy exhibited a higher amplitude and frequency than those at the reattachment and secondary eddy zones, indicating a stronger and more frequent pattern of eddy pulsations at the separation and primary eddy zones and a lower frequency and less pronounced pattern at the secondary eddy and reattachment zones. At the near-surface grid cells, the power spectra reflected the presence of frequencies with higher energy compared to those observed at six and two-tenths of the total depth. The low-frequency components of the power spectra showed dominant eddy pulsations in the flow, while the higher frequencies showed smaller fluctuations. These eddy pulsation patterns are also consistent with studies conducted by Rubin and McDonald (1995).

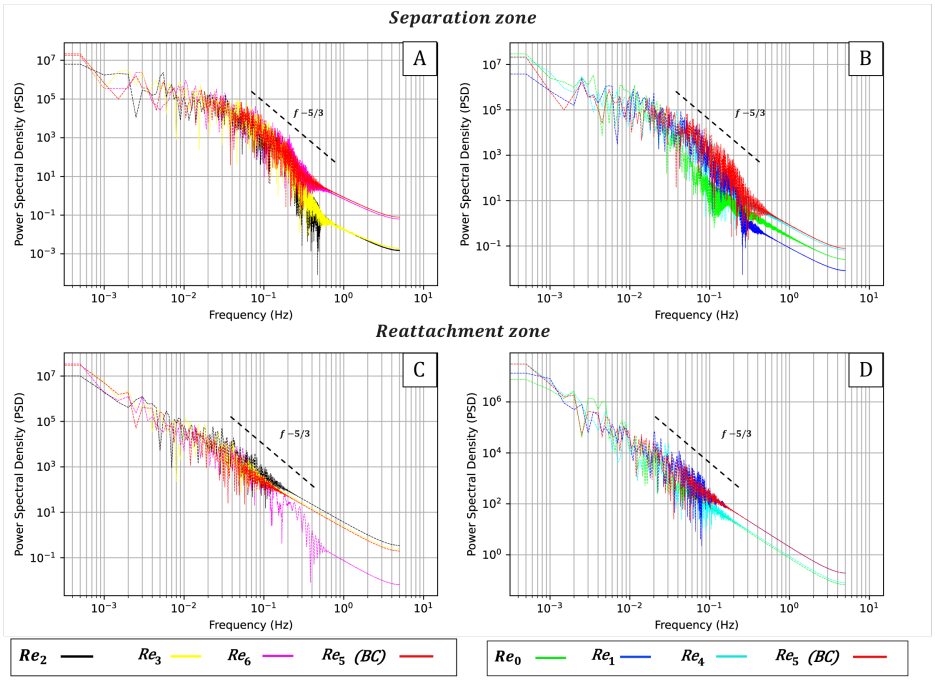

FIGURE 9 Power Spectral Density (PSD) of the velocity fluctuations $(m/s)^2 Hz^{-1}$) versus the frequency (Hz) at six-tenths of the channel depth grid cells at A) and B) Separation zone for site W; C) and D) Reattachment zone for site Z.

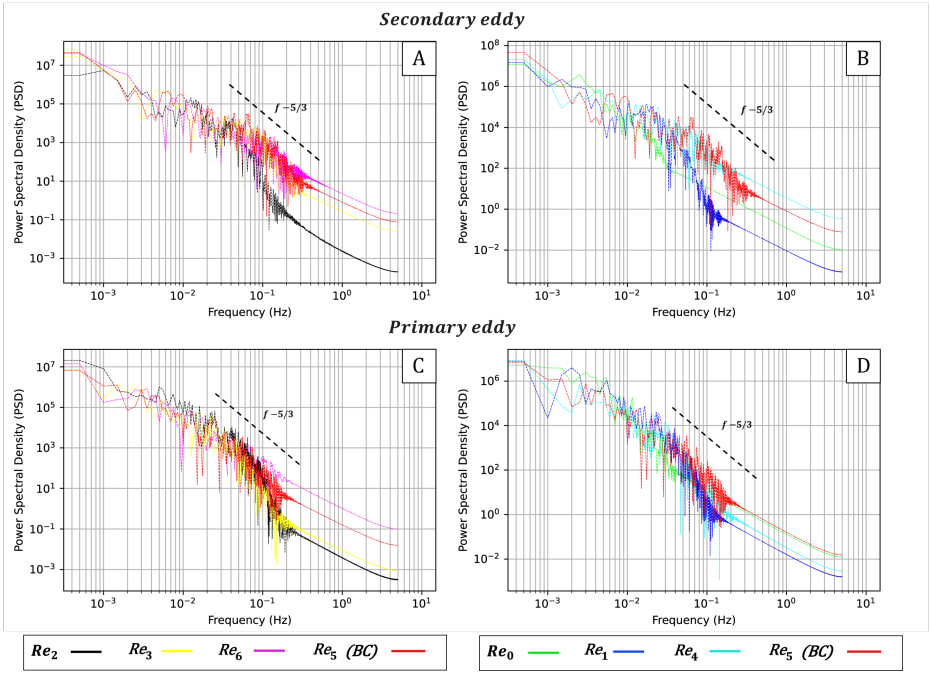

FIGURE 10 PSD of the velocity fluctuations $(m/s)^2 Hz^{-1}$) versus the frequency (Hz) at six-tenths of the channel depth grid cells at A) and B) Secondary eddy for site X , C) and D) Primary eddy for site Y.

The power spectrum was associated with three regions of different spectral behavior in the separation zone, primary and secondary eddy (Figures 9 A and B, Figures 10 A, B, C, and D). The signal exhibited a flat Power Spectral Density (PSD) across all frequencies below 0.001 Hz, indicating white noise in that frequency region. The second region, between 0.001 and 0.5 Hz, corresponds to a Brownian walk, representing the random motion of particles influenced by turbulent eddies at larger scales and molecular diffusion at smaller scales. The power spectrum in this range captures the energy transfer across scales and highlights the dominance of dissipative, Brownian-like motion at the smallest scales. In the third region, with frequencies

higher than 0.5 Hz, there is a change to a flatter spectrum, where the power or energy distribution is more uniform at different frequencies. A spectrum flattening is observed in the reattachment zone along the power spectrum (Figures 9 C and D). In the region where turbulent flow cascades dissipated within the inertial range, high-energy frequency fluctuations were characterized by a well-defined slope consistent with the Kolmogorov exponent of -5/3.

The PSD of velocity fluctuations captured frequencies ranging from 0.001 to 5 Hz in all the computational domain resolutions. In the separation zone, at a frequency of 5 Hz, the finest computational resolutions, Re_4 Re_5 and Re_6, captured energy levels of $0.1(m/s)^2 Hz^{-1}$, while resolutions Re_2 and Re_3 captured an energy level of $0.001(m/s)^2 Hz^{-1}$ at the same frequency (see Figures 10 A, and B). These results revealed that at this location, the finer resolutions (Re_4, Re_5, and Re_6) captured 100 times more energy at a frequency of 5 Hz than the coarser resolutions (Re_2 and Re_3) at the same location. Similar behavior was observed in resolutions Re_0 and Re_1, where energies less than 0.089 $(m/s)^2 Hz^{-1}$ were captured at a frequency of 5 Hz (Figure 10 B). In the primary eddy zone at site X, it was observed that the finest resolution Re_6 showed an energy value of 0.1 $(m/s)^2 Hz^{-1}$ at a frequency of 5 Hz, followed by the resolution Re_5, which captured an approximate energy value of 0.01 $(m/s)^2 Hz^{-1}$. However, at resolutions of Re_2 and Re_3, the energy values at a frequency of 5 Hz were below 10^{-3} $(m/s)^2 Hz^{-1}$, as shown in Figure 10 C. The resolutions Re_0, Re_1, and Re_4 showed energy values lower than 0.01 $(m/s)^2 Hz^{-1}$ (Figure 10 D). The PSD analysis of the secondary eddy at the same frequency revealed an energy value of 0.1 $(m/s)^2 Hz^{-1}$ for Re_5, while the resolutions Re_4 and Re_6 obtained energy values close to $0.5(m/s)^2 Hz^{-1}$. The resolutions Re_0 and Re_1 captured values below 0.01 $(m/s)^2 Hz^{-1}$, and Re_2 had values below 0.001 $(m/s)^2 Hz^{-1}$. The resolutions Re_3, Re_4, Re_5, and Re_6 captured higher energy values at higher frequencies in the PSD than those captured by the resolutions Re_0, Re_1, and Re_2; these frequencies correspond to smaller-scale fluctuations with shorter wavelengths.

In terms of the TKE spectrum, the higher resolution computational domains (Re_4 and Re_6) exhibited a closer fit to the results obtained for the benchmark case in contrast to the low-resolution outputs (Re_0, Re_1, Re_2, and Re_3), as shown in 11 . The energy spectra for the separation and reattachment zone (Figure 11 A and Figure A1) and primary and secondary eddy (Figures 11 C and D) showed high energy accumulation on the largest scales. In contrast, on small scales, where the spatial frequency of the eddy was greater than 10 m^{-1}, the energy was overdissipated. A flattened profile was observed in the separation zone up to the rapid decreased in turbulence kinetic energy at the 10 m wavelength (See Figure11 A). In contrast, for the reattachment zone, primary and secondary eddy, the kinetic energy spectrum decreases smoothly up to a wavenumber of 8 m^{-1} (see Figures 11 B, C and D). At wavenumbers greater than 8 m^{-1}, there is a high dissipation of kinetic energy; in this range the energy showed values within 10^{-3} and 10^{-13} m^2/s^2. This pattern was observed for all the sites (W, X, Y, and Z). The results demonstrated that resolutions Re_6 and Re_4 captured smaller scales of turbulence and provided a more accurate representation of the TKE spectrum compared to the benchmark case scenario Re_5. The TKE spectrum exhibited a range of scales, from large-scale motions associated with the overall flow behavior to small-scale motions associated with highly localized turbulence for all the computational domain resolutions.

4.2.2 Wavelet spectrum analysis

In this research, wavelet analysis assessed the capabilities of six computational domain resolutions (Re_0, Re_1, Re_2, Re_3, Re_4, and Re_6) to capture eddy pulsations at spatial-temporal scales, compared to the benchmark case scenario (Re_5). The theoretical foundations and equations of the wavelet theory can be found in Torrence and Compo (1998) and Lee and Yamamoto (1994). The Python wavelet software based on Torrence and Compo (1998) was used to compute the wavelet power spectrum. The wavelet transform was applied to the time series of velocity fluctuations at the sites W, X, Y, and Z at six-tenths of the channel depth grid cells, located at the separation zone, primary and secondary eddy and the reattachment point, respectively (see Figure 8 B). These sites were located in the mass transfer exchange from the main channel to the eddy zone. This approach analyzes the periodicity of velocity fluctuations along the plane or intersection of the main channel and the separation zone where sediment import and export occur. Wavelet time-frequency analysis helped identify fluctuations that produce kinetic energy on larger scales and capture localized processes at smaller scales that contain high-energy events in the time series.

The frequency spectrum of the Wavelet Power Spectral Density (WPSD) displayed the relationship between velocity fluctuation amplitude and frequency, as revealed by the wavelet transform. Figures 12 and 13 show the power spectrum of the magnitude of the simulated velocity in the near surface and six-tenths of the channel depth grid cells, respectively, for the domain resolutions Re_0 (coarser grid) and Re_5 (benchmark case) at separation (see Figures 12 A and B, Figures 13 A and

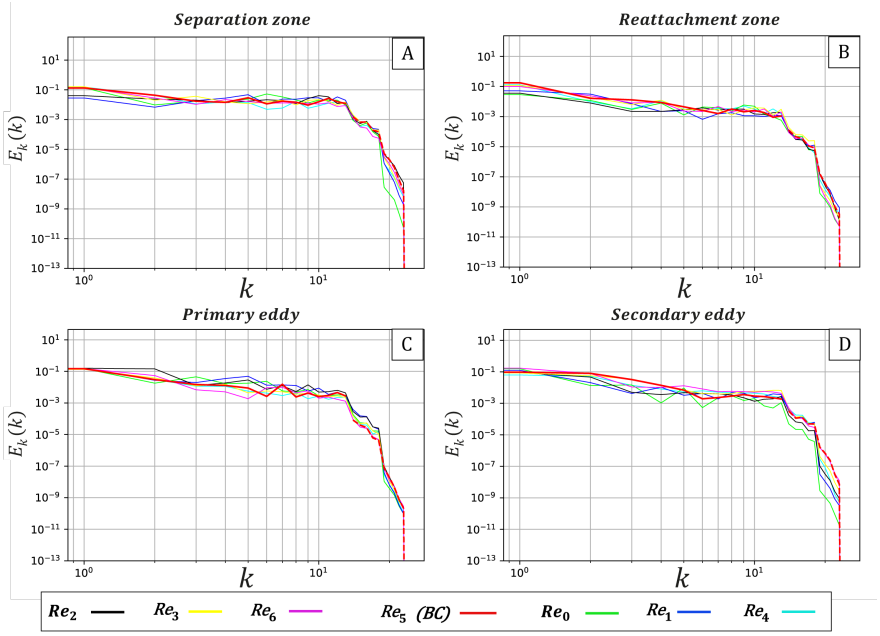

FIGURE 11 Turbulent kinetic energy spectrum for the velocity field in m^2/s^2 versus the wavenumber k in m at six-tenths of the channel depth grid cells in sites W, X, Y, and Z (defined in Figure 5).

B) and in the reattachment zone (see Figures 12 C and D, Figures 13 C and D). The wavelet spectrum of velocity was used to compare the ability of the six computational domain resolutions to capture eddy pulsations at spatial-temporal scales to the benchmark case scenario. At six-tenths of the channel depth grid cells, the results showed a 12-min periodic signal in the reattachment zone (see Figures 12 C and D), which was more noticeable during the 15 to 20-min simulation for the resolution Re_0, in contrast to the resolution Re_5 showed a 17-min signal featured during the 19 to 30-min simulation. In the separation zone (see Figures 12 A and B), a strong 5-min periodic signal was captured and exhibited from 10 to 25 min in resolution Re_0. For resolution Re_5, this signal became stronger and more noticeable during 15 to 30 min. The results indicate a trend for higher values and frequent eddy pulsations at the separation zones. In contrast, the eddy pulsations at the reattachment zones are less pronounced and occur at lower frequencies.

Figures 13 A and B showed the wavelet power spectrum in the near-surface grid cells in the separation zone. The resolution Re_0 (Figure 13 A) indicated a strong periodicity with signals of 2-min and 4-min period at 10 to 15 min and 20 to 25 min, respectively. On the other hand, the resolution Re_5 (Figure 13 B) showed a less prominent signal with a higher periodicity between 10 to 20 min, oscillating between periods from 0.25 to 4 min. In the reattachment zone, the wavelet power spectrum in the cells of the near-surface grid cells is shown in Figures 13 C and D. The resolution Re_0 (Figure 13 C) indicated a higher periodic signal from 10 to 20 min of simulation than a lower signal from 20 to 30 min. Conversely, the resolution Re_5 (Figure 13 D) showed a weaker signal from 15 to 30-min. The findings demonstrated that using higher grid resolution (Re_5) enabled the detection of smaller length scales, resulting in a more accurate representation of turbulence structures and a better identification of the patterns in the wavelet spectrum.

4.3 Spatiotemporal distributed analysis

We selected four forecasting metrics (RMSE, NSE, KL-divergence, and GCI) because they provide a holistic diagnosis of the model results. Model validation based on just one or two metrics could lead to misinterpretation, as they evaluate different characteristics of the data distribution. Using four metrics helps compensate for shortcomings in individual metrics. For instances, the (RMSE) is easy to interpret and measures overall model accuracy but is sensitive to outliers and does not distinguish between error types. The NSE effectively compares model predictions to observed data but is also sensitive to extreme values and fails to differentiate between over- and underestimation errors. Kullback-Leibler (K-L) divergence is advantageous for measuring the difference between two probability distributions, providing a clear and interpretable metric for comparing distributions in various fields such as information theory and machine learning. It is beneficial for applications in model selection and entropy

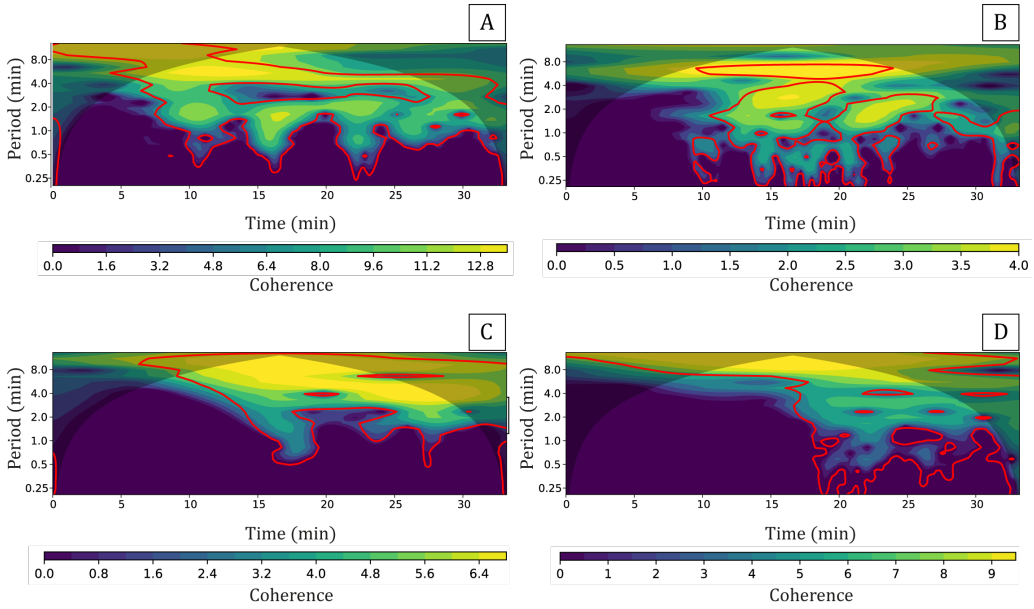

FIGURE 12 Wavelet velocity power spectrum at six-tenths of the channel depth grid cells for A) domain resolution Re_0 in the separation zone (site W). B) domain resolution Re_5 (benchmark case) in the separation zone (site W). C) domain resolution Re_0 in the reattachment zone (site Z). And D) domain resolution Re_5 in the reattachment zone (site Z). Note: the thick red-colored contour lines represent areas with a confidence level greater than 95% for a red-noise process with a lag-1 coefficient of 0.9. The shaded sections located on both ends of the lines indicate the cone of influence.

calculations. However, if the Probability Density Function (PDF) of the benchmark case scenario has zero values when the it is compared the evaluated coarser resolution, the divergence becomes infinite, complicating the interpretation of its result. The Grid Convergence Index (GCI) is advantageous for providing a standardized estimate of discretization error in numerical simulations, helping to assess grid independence. It offers a systematic approach to quantify convergence and can be applied across various computational domains. However the GCI has several shortcomings, including its dependence on grid quality and the requirement for a consistent grid refinement ratio. It typically assumes second-order accuracy, referring to the rate at which the numerical error decreases as the grid is refined, which can lead to inaccuracies if this condition is not met. Additionally, GCI provides a single error estimate that may not capture the full range of spatial changes in the eddy structures.

4.3.1 RMSE statistical metric values

A statistical method based on the RMSE metric was employed to evaluate the accuracy of the model's representation of flow behavior, hydraulic characteristics, primary and secondary flows, shear layers, and primary and secondary eddies. A spatiotemporal distribution analysis was performed to study the distribution of the RMSE values over space and time. It involves spatial analysis and data visualization of the RMSE variations across different spatial locations along the EM transect for each domain resolution. The EM transect was analyzed spatio-temporally integrated using 20,000 randomly distributed point probes. This random sample was generated using the ArcGIS spatial random sampling tool, creating 20,000 random point features inside the EM transect polygon feature (see Figure 14) (Rees 2014). The ArcGIS spatial join tool was used to spatially match the created random sample of points with the center points of each cell of the computational domain based on their relative spatial locations assigning each random point a coordinate within the computational domain corresponding to the center of the nearest cell.

The magnitude of the simulated velocity values was collected for each computational domain in 33 minutes at a time step of 15 seconds. As a result, 20,000 time series of velocity magnitude for each domain were obtained. The time series were used to calculate a point-to-point value of the RMSE between the coarser simulated domain resolutions and the benchmark case simulated velocity values. The resulting data were then employed to create an interpolated surface of spatially distributed RMSE along the EM transect, enabling the assessment of the model's grid resolution and forecasting capabilities by quantifying the errors between the simulated and benchmark case's spatially distributed velocity field.

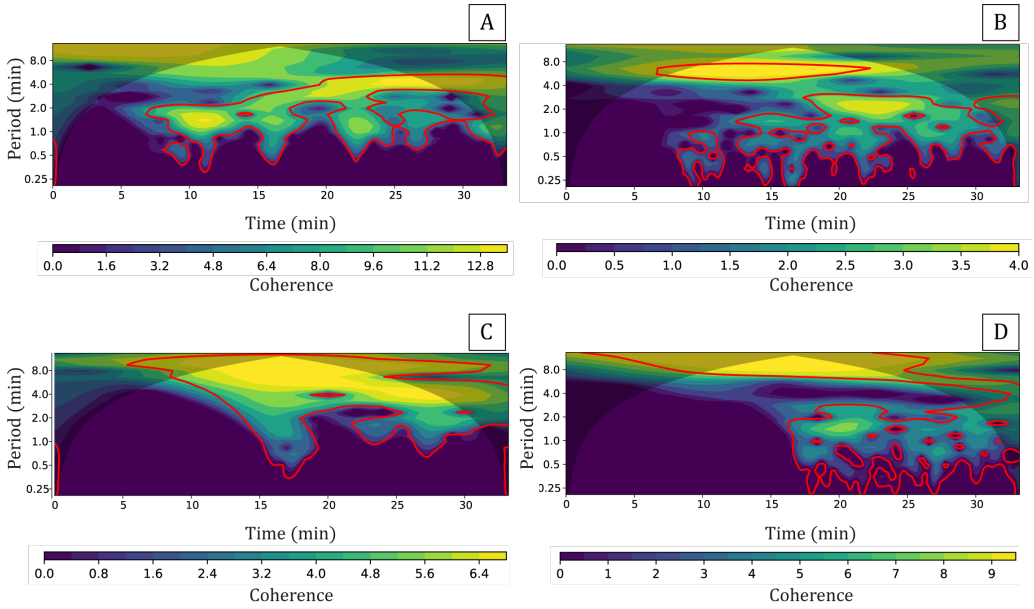

FIGURE 13 Wavelet power spectrum of velocity at near-surface grid cells for A) domain resolution Re_0 in the separation zone (site W). B) domain resolution Re_5 (benchmark case) in the separation zone (site W). C) domain resolution Re_0 in the reattachment zone (site Z). And D) domain resolution Re_5 in the reattachment zone (site Z). The thick, red-colored contour lines represent areas with a confidence level greater than 95% for a red-noise process with a lag-1 coefficient of 0.9. The shaded sections located on both ends of the lines indicate the cone of influence.

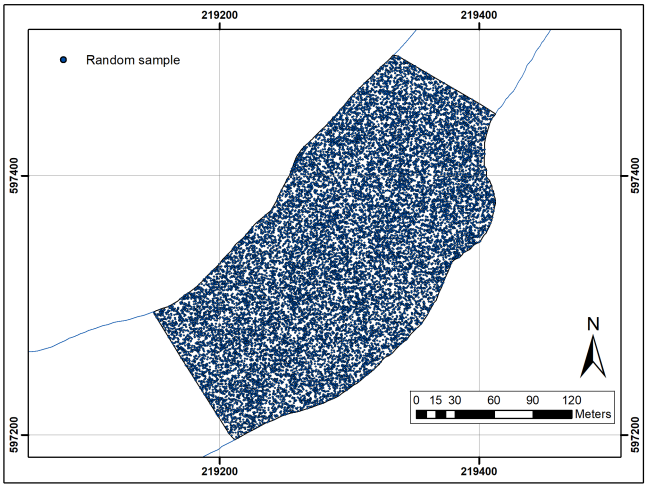

FIGURE 14 Random spatial sampling coordinate points in the Eminence Break (EM) transect.

The distribution of RMSE values across the area were found on surfaces obtained at the near-surface and six-tenths of the channel depth grid cells, as illustrated in Figure 15 and Figure 16 , respectively. The results for the near-surface grid cells indicated that at low domain resolutions (Re_0, Re_1, and Re_2), the main channel, the separation, and reattachment bars had the highest RMSE values ranging from 0.65 to 3.8 m/s. The RMSE values in the lateral separation zone and the primary eddy ranged from 0.09 to 0.44 m/s, respectively, while the secondary eddy zone had RMSE values between 0.25 and 0.44 m/s (see Figure 15 A, B and C). At medium and high resolutions (Re_3, Re_4, and Re_6), lower RMSE values were found throughout the area. The smallest values were located downstream of the lateral separation zone, near the reattachment bar, and close to the primary eddy. These values ranged between 0.05 and 0.24 m/s (see Figures 15 D, E, and F). The highest RMSE values were located along the main channel ranging from 0.65 to 1.2 m/s (see Figure 15 F).

The results indicated that in the near-surface grid cells, lower RMSE values were observed along the lateral separation zone compared to the results obtained at six-tenths of the channel depth grid cells, except for resolution Re_3 which showed higher RMSE values at this location (Figure 16). The lateral separation zone and primary eddy had RMSE values ranging from 0.09 to 0.44 m/s, while the secondary eddy zone had RMSE values between 0.25 and 0.44 m/s (Figure 16 A, B, and C); at these low resolutions (Re_0, Re_1, and Re_2), the main channel and the separation and reattachment bars had the highest RMSE values ranging from 0.65 to 3.8 m/s (see Figure 16 A). At the six-tenth location of the channel depth grid cells, Figure 16 showed lower RMSE values throughout the area at medium and high resolutions (Re_3, Re_4, and Re_6), with the smallest values located in the southern region of the lateral separation zone, near the reattachment bar (see Figures 16 D and E), and close to the primary eddy (Figure 16 F). These values ranged from 0.02 to 0.34 m/s. The highest RMSE values were found along the main channel, ranging from 0.35 to 0.64 m/s (Figures 16 E and F).

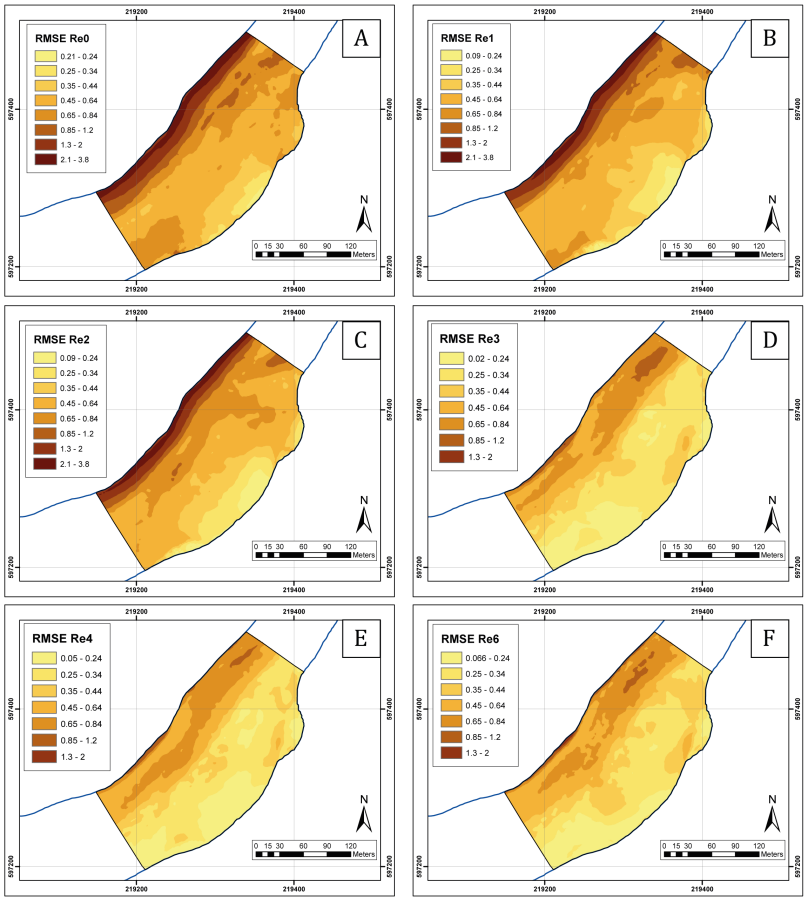

FIGURE 15 RMSE surface values for domain resolutions: A) Re_0, B) Re_1, C) Re_2, D) Re_3, E) Re_4, and F) Re_6 at near-surface grid cells.

Tables B1 and B2 summarized the percentages of the total area corresponding to each range of RMSE values for each computational domain in the six-tenths generated from the channel depth and near-surface grid cells. For the RMSE values located in the near-surface grid cells, the 97.3% of the total area of the RMSE surfaces for resolutions Re_4 and Re_6 showed a value of less than 0.84 m/s, in the surface Re_0, the 90% of the area registered RMSE values less than 2 m/s. Regarding the resolutions Re_1 and Re_2, 90% of the total area showed RMSE values less than 1.2 m/s, and in the resolution Re_3, approximately 79.1% of the total area had RMSE values less than 0.84 m/s (Appendix B).

Analysis of RMSE values in six-tenths of the channels depth grid cells revealed that at resolutions Re_4 and Re_6, approximately 98% of the total area had values lower than 0.84 m/s, primarily located along the lateral separation zone close to the right river bank. In resolutions, Re_0 and Re_1, the 89% of the total area showed RMSE values of less than 1.2 m/s. For the resolutions Re_2 and Re_3, 87% of the total area showed RMSE values of less than 0.84 m/s. For domain resolutions higher than

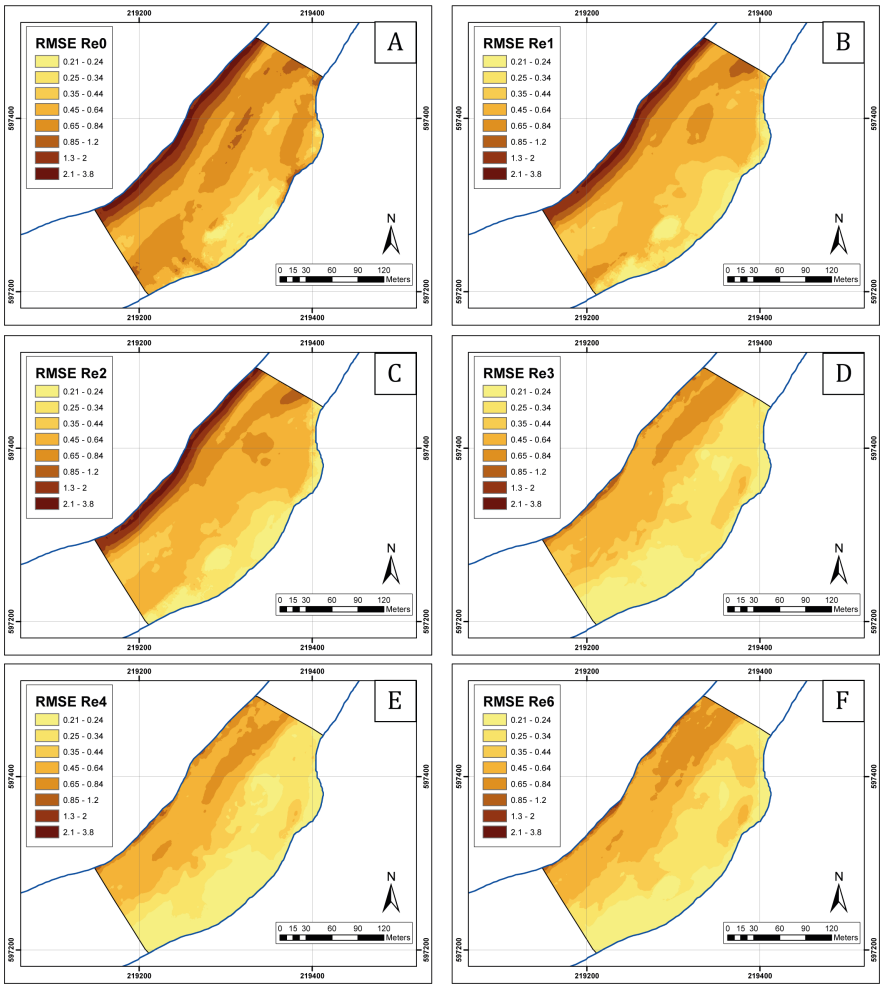

FIGURE 16 RMSE surface values for domain resolutions: A) Re_0, B) Re_1, C) Re_2, D) Re_3, E) Re_4, and F) Re_6 at six-tenths of the channel depth grid cells.

Re_3, the RMSE values for over 60% of the total area of the EM transect were less than or equal to 0.44 m/s.

The results showed that the RMSE values for the near-surface cells and six-tenths of the channel depth grid were relatively small, despite the wide range of measured velocities along the river transect ranging from 0.13 to 4 m/s in the base case scenario (16 and 17). However, the resolutions Re_3, Re_4, and Re_6 exhibited the lowest RMSE values compared to Re_0, Re_1, and Re_2. In the near-surface grid cells, the RMSE values in the lateral recirculation zone for Re_3 were similar to those obtained in finer resolutions such as Re_4 and Re_6, ranging from 0.05 to 0.44 m/s. These values were also observed downstream of the lateral separation.

Similar results were observed in the region corresponding to the secondary eddy, with RMSE values ranging from 0.35 to 0.64 m/s for resolutions Re_3, Re_4, and Re_6. The RMSE results remained relatively the same for the Re_3 resolution, obtaining similar values for finer resolutions Re_4 and Re_6 (see Figure 17 A and B). These results suggest that when the computational resolution is at least twice as coarse as the benchmark case resolutions, no significant differences were observed in the RMSE values for the lateral and downstream area of the lateral recirculation zone. These findings indicated that the RMSE became insensitive to grid refinement after reaching domain resolution Re_3.

4.3.2 KL - divergence statistical skill metric

KL - divergence was employed to measure the proximity between the benchmark case and the generated probability distributions within the computational domains. These measures are known as information divergence and relative entropy (Joyce

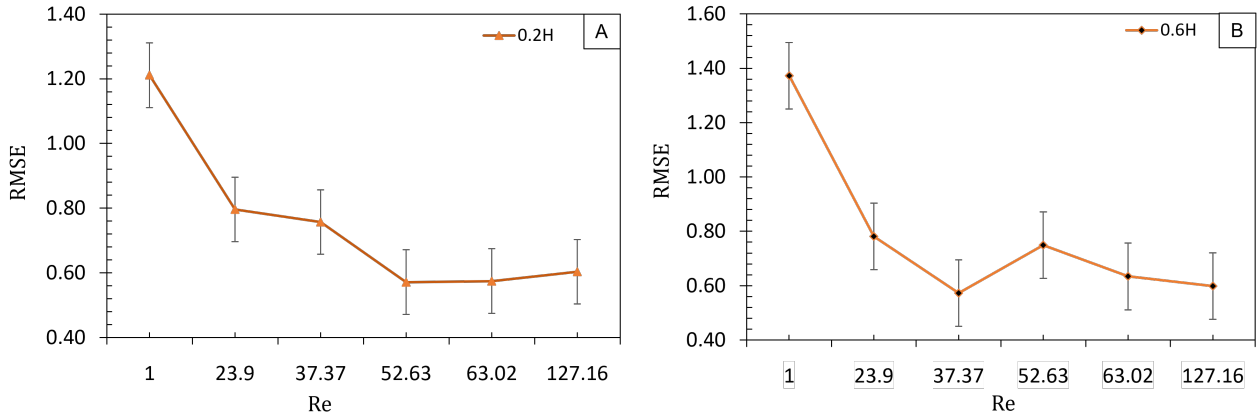

FIGURE 17 (A) RMSE results located at near-surface grid cells. (B) RMSE results located at six-tenths of the channel depth. X-axis shows the computational domain resolution (Re), and the y-axis RMSE values for each domain resolution.

2011). Thus, the information was measured as a change in the probability distributions (Nearing and Gupta 2015). For distributions P and Q of a continuous random variable, the relative entropy is given by: $D(P\|Q) = \int_{\mathbb{R}^d} p(\mathbf{x}) \log \frac{p(\mathbf{x})}{q(\mathbf{x})} d\mathbf{x} \geq 0.$, where p and q denote the probability densities of P and Q. P represents the "true" distribution of the data given by the simulation results of the benchmark case, while Q represents each constructed domain resolution that approximates P (Joyce 2011). Previous studies have used the KL - divergence as a metric of the information obtained from the data to optimize the experimental design (Lomeli et al. 2021; Chaloner and Verdinelli 1995). This metric was commonly employed in information theory as an equivalent to mutual information gain (Ryan et al. 2016; Huber HA 2023). Other researchers employed KL - divergence to quantify information loss (Smith et al. 2006). In this research, the KL - divergence served as a means to connect estimation theory and model selection, effectively bringing them together within a shared optimization framework. The KL - divergence function was used as a metric to quantify the information loss as the difference between the prior and posterior probability model distributions for all domain resolutions.

A sample of 20,000 points randomly distributed along the EM transect of interest was used to calculate the KL - divergence for each computational domain. This random sample of points was generated using the ArcGIS spatial random sampling tool, this tool created 20,000 random points generated inside the EM transect polygon feature (Rees 2014). The values of the time-averaged velocity associated with each point were obtained for each resolution of the computational domain. The sample points were located at depths of two-tenths (near-surface grid cells) and six-tenths (average velocity of the velocity profile). The Python scipy library was employed to compute the relative entropy.

The probability density functions were found to be positively skewed across all the computational domain resolutions. At the near-surface grid cells (Figure 18), the KL-divergence showed values between 124 and 221 (Table 4) for resolutions Re_0, Re_1, and Re_2, as shown in Figures 18 A, B, and C. For resolutions Re_3, Re_4, and Re_6, the KL- divergence values were between 3.4 and 8.7. The large KL - divergence values obtained for resolutions Re_0, Re_1, and Re_2 compared to those obtained for the benchmark case indicated a large discrepancy between these resolution distributions and the benchmark case. Similar behavior was observed in six-tenths of the channel depth grid cells (Figure 20 and Table 3), where the KL - divergence for resolutions Re_3, Re_4, and Re_6 was between 1.99 and 8.

Figures 18 A, B, and C; and Figures 19 A, B, and C showed that the PDF curves for domain resolutions Re_3, Re_4, and Re_6 followed a similar distribution pattern observed for the benchmark case Re_5. For resolutions Re_3, Re_4, Re_5, and Re_6 PDFs the mean and variance values were 0.15 m / s and 0.020 m / s, respectively (Table C3 , Appendix C). These values did not change significantly with posterior grid refinement, indicating that KL-divergence results were insensitive to further refinement beyond Re_3. The findings suggested that the use of moment-based filters, such as mean and variance, is an optimal approach that minimizes information loss in CFD computations rather than just arbitrary techniques. These results are significant for minimum divergence filtering algorithms, which aim to minimize KL- divergence rather than MSE.

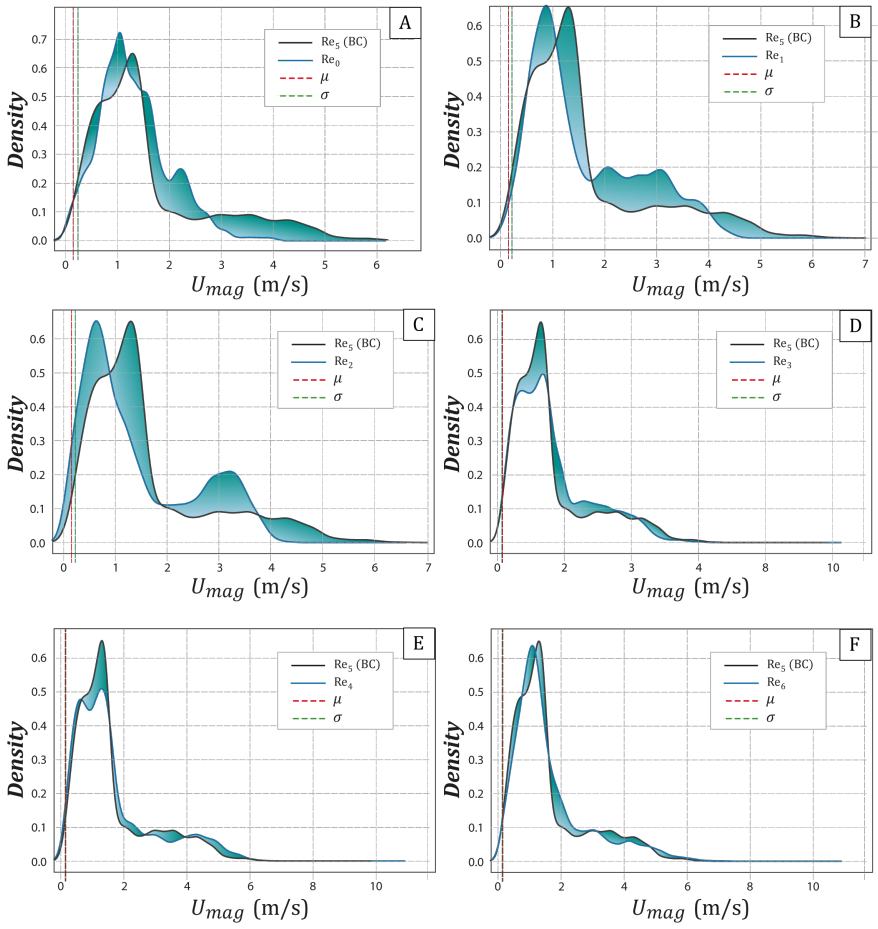

FIGURE 18 Representation of the KL-divergence at near-surface grid cells for A) resolution Re_0, B) resolution Re_1, C) resolution Re_2, D) resolution Re_3, E) resolution Re_4, F) resolution Re_6. Note: the divergence areas were marked in blue.

The KL-divergence can also be interpreted in terms of information loss. This information loss is known as the relative entropy between the benchmark case Re_5 and the domain resolutions Re_0, Re_1, Re_2, Re_3, Re_4, and Re_6. Thus, the finer grid resolutions (Re_3, Re_4, and Re_6) at both sites near-surface grid cells and six-tenths of the channel depth grid cells (see Figures 18 D, e, and f; and Figures 19 D, E, and F) exhibited a value of KL-divergence between 2 and 8.73. These values represent the information lost when using the distributions (Re_3, Re_4, and Re_6) to approximate the benchmark case distribution Re_5. However, the results were relatively low compared to those obtained for resolutions Re_0, Re_1, and Re_2 (Figures 18 A, B and C; and Figures 19 A, B, and C). In these resolutions, the computational domain poorly captured the details of the velocity field, resulting in higher KL-divergence values and hence a higher amount of information lost.

Domain resolutions with less information loss were Re_4 with a value of 2 at six-tenths of the channel depth grid cells and resolution Re_3 at near-surface grid cells, with a value of 3.4 (Tables 3 and 4). The results in Figures 20 A and B showed that the resolutions Re_3 and Re_4 led to a more accurate approximation of the probability distributions between the simulated computational domains and the reference case, which, in turn, can reduce the amount of information lost when using one distribution to approximate another.

4.3.3 NSE efficiency coefficient statistical skill metric

The NSE coefficient is commonly used to evaluate hydrological or environmental models. Assesses residual variance relative to measured variance and has a range of $[-\infty, 1]$, with 1 indicating a complete correspondence between the modeled and observed data (Nash and Sutcliffe 1970; Gupta et al. 2009). The method of calculation is described in $E_f = 1 - \frac{\sum_{i=1}^{n}(y_i - \hat{y}_i)^2}{\sum_{i=1}^{n}(y_i - \bar{y})^2}$, where y_i is the observed value, $\hat{y}_i$ is the predicted value, $\bar{y}$ is the observed average and n is the sample size. NSE was used as E_f

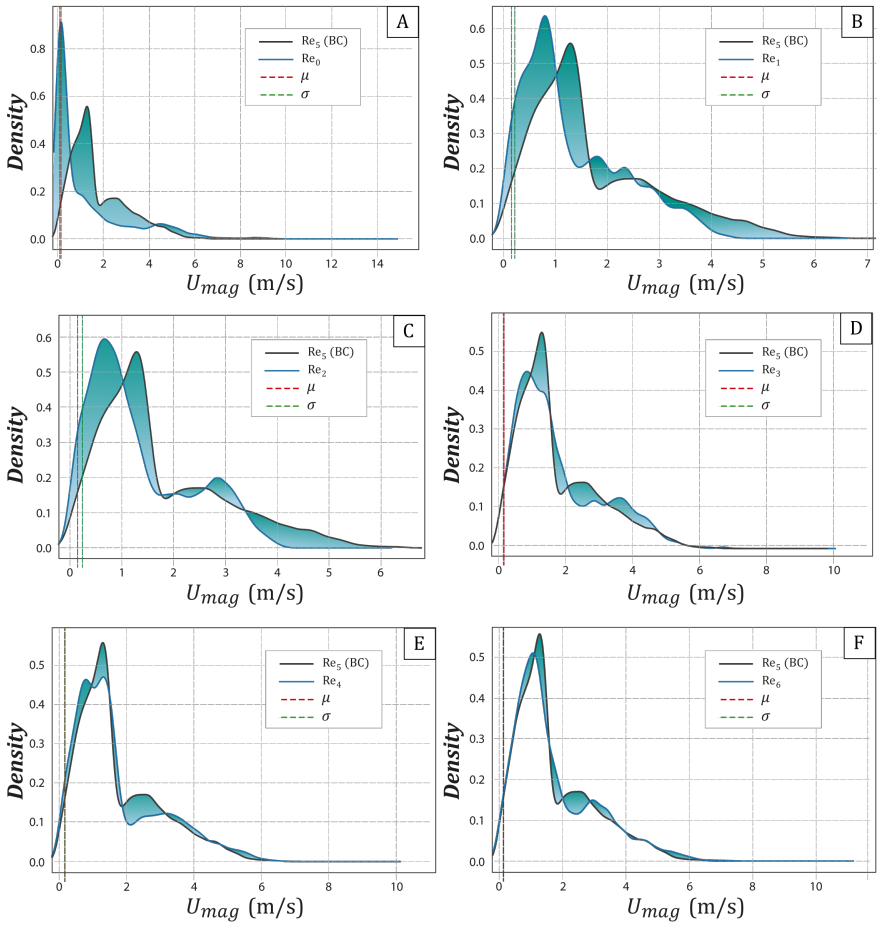

FIGURE 19 Representation of the KL-divergence at six-tenths of the channel depth grid cells for A) resolution Re_0, B) resolution Re_1, C) resolution Re_2, D) Resolution Re_3, E) resolution Re_4, F) resolution Re_6, the divergence areas were marked in blue.

TABLE 3 RMSE, NSE, and KL-divergence results of the random point probe samples located at six-tenths of channel depth grid cells for resolutions: Re_0, Re_1, Re_2, Re_3, Re_4, and Re_6

	Six-tenths of the channel depth grid cells					
Resolutions	Re_0	Re_1	Re_2	Re_3	Re_4	Re_6
KL-divergence	204	106.04	147	5.76	1.99	8
NSE	0.583	0.865	0.927	0.876	0.911	0.921
RMSE	1.37	0.78	0.57	0.749	0.634	0.60

to evaluate the accuracy of the results obtained for each grid resolution. To assess how well the average velocity values of each domain resolution represent the benchmark case average velocity results, the NSE was calculated for a randomly distributed sample of 20,000 points located near the surface and six-tenths of the channel depth grid cells. These points were matched with the time-averaged velocity values. When the value of NSE is closer to 1, the accuracy and stability of the model simulation results are higher. Conversely, when the simulation results are closer to 0, the average value of the measured samples is also closer, making the overall model more reliable, but the process error is greater. However, if the value of NSE is less than 0, the simulation results of the model cannot be considered credible (Moriasi et al. 2007; McCuen et al. 2006).

Figures 20 C and D show the NSE results of a randomly distributed sample of 20,000 points in the near-surface grid cells and six-tenths of the channel depth grid cells. For resolutions Re_0, Re_1, and Re_2, it was observed that the NSE values increased

TABLE 4 RMSE, NSE, and KL-divergence results of the random point probe samples located in the near-surface grid cells for resolutions: Re_0, Re_1, Re_2, Re_3, Re_4, and Re_6

	Near-surface grid cells					
Resolutions	Re_0	Re_1	Re_2	Re_3	Re_4	Re_6
KL-divergence	221.05	124.22	141.89	3.39	8.73	3.91
NSE	-0.012	0.563	0.605	0.775	0.772	0.749
RMSE	1.21	0.8	0.76	0.571	0.574	0.60

rapidly, from -0.012 to 0.605 for near-surface grid cells and values from 0.583 to 0.927 for cells located six-tenths of the channel depth. The values taken by the NSE for resolutions Re_3, Re_4, and Re_6 remained in the range between 0.775 and 0.749 for near-surface grid cells and between 0.876 and 0.921 for cells located six-tenths of the channel depth grid cells. The findings indicated that the value of the NSE coefficient was not affected by the mesh resolution after Re_3, as there was no significant variation in the results for resolutions Re_4 to Re_6. After reaching the grid resolution of Re_3, the value of the NSE coefficient became insensitive to further grid refinement. Therefore, any further refinement of the grid would not significantly impact the NSE results.

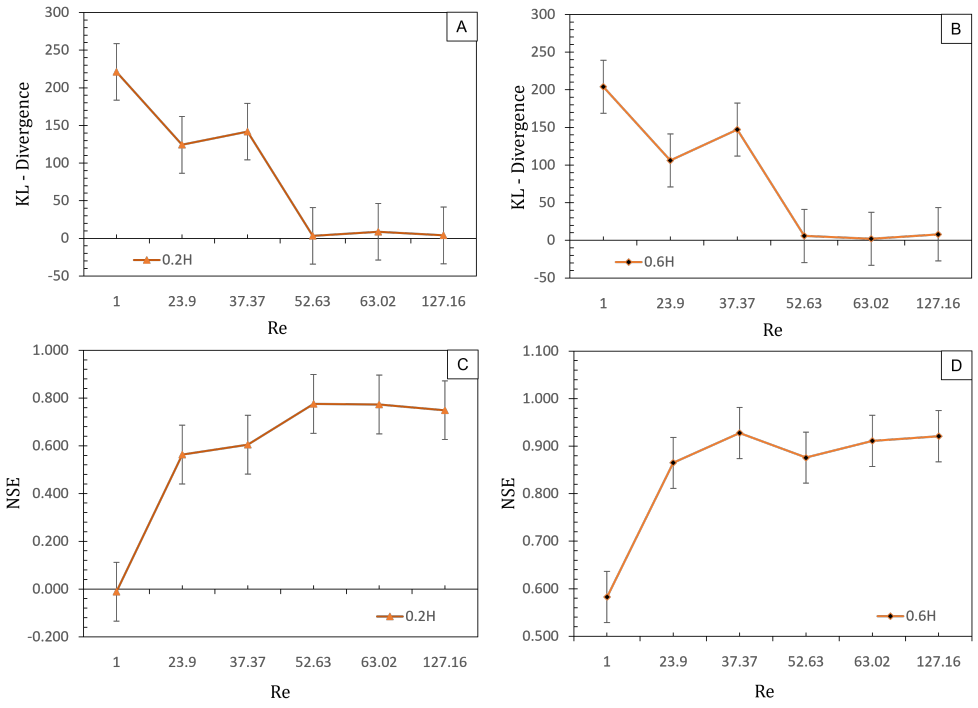

FIGURE 20 (A) KL-divergence at near-surface grid cells. (B) KL- divergence at six-tenths of the channel depth grid cells. (C) NSE coefficient at near-surface grid cells. And (D) NSE coefficient at six-tenths of the channel depth grid cells.

4.3.4 Grid convergence index (GCI) analysis

The GCI employs Richardson extrapolation given by: $f_e \cong f_1 + \frac{f_1 - f_2}{r^p - 1}$, where f_1 and f_2 represent numerical solutions for the analyzed variables on two distinct grids, with discrete spacings denoted as h_1 (fine grid) and h_2 (coarse grid), respectively. $r = \frac{h_2}{h_1}$ represents the grid refinement ratio and p is the accuracy order of the discretization scheme. Richardson extrapolation aims to approximate the exact solution (f_e) by using numerical solutions f_1 and f_2. The relative numerical error (E_0) between the finest grid solution and f_e is described in $E_0 = \frac{\varepsilon}{r^p - 1}$. The relative error between f_1 and f_2, is represented by ε defined in: $\varepsilon = \frac{f_1 - f_2}{f_1}$.

The numerical error E_0 is multiplied by a safety factor F_s and the GCI is given by $GCI = F_s \frac{|\varepsilon|}{r^p - 1}$. According to Roache (1998), when more than two grids are used, the safety factor is set to 1.25. This approach allows for an estimation of the exact solution. The solution to this method is accurate only in an asymptotic range, which is achieved when a smaller grid cell does not change the resolved quantities (Coelho and Argain 1997; Phillips and Roy 2014; Roache and Knupp 1993). The GCI estimator assesses the precision of the grid scheme by determining the percentage error between the calculated values and an asymptotic numerical value, which is the true solution. This is accomplished by comparing the results obtained using the finest grid, which serves as the reference grid, with those obtained using coarser grids. The uncertainty of this metric is estimated by multiplying the absolute value of the Richardson extrapolation error by a safety factor determined based on knowledge of the nearness to the asymptotic range (Phillips and Roy 2014; Roy 2005; Roache 1998).

The present GCI analysis employs the method proposed by Celik et al. (2008) to minimize the discretization error to optimize modeling performance. (Baker et al. 2020a; Eça and Hoekstra 2014; Samion et al. 2019). Three grid resolutions, denoted as Re_6, Re_5, and Re_4, were created to conduct the computation. These grids are called fine, middle and coarse, consisting of N1, N2 and N3 elements. Initially, the average spacing for each grid (h_i) was determined by $h_i = \left[\frac{1}{N_i}\sum_{j=1}^{N_i} \Delta V_j\right]^{1/3}$, where ΔV_j denotes the volume of each grid element. The observed accuracy order p was determined after calculating the grid refinement ratios $r_{54} = \frac{h_5}{h_4}$ and $r_{65} = \frac{h_6}{h_5}$. The GCI indicated the change in the solution with further refinement and determined how far the solution was from the asymptotic range. A small value of GCI means that the results are within the asymptotic range (Baker et al. 2020b).

The GCI study employed three different grids, as listed in Table 5 . The least refined grid contained about 3.5 million elements, while the most refined had approximately 7.2 million elements. Refinement ratios, r, exceeding 1.1 were utilized to generate all grid resolutions (Celik et al. 2008). In this study, the time step was set to equal to $\Delta = 0.1$ seconds. The CFL stability condition denoted by $CFL = \frac{u\Delta t}{h} \leq 1$, was considered when performing the mesh independence study. This condition guaranteed not only stability but also greater numerical accuracy. Estimation of the exact solution in the GCI method was based on a series of numerical computations to estimate the error in the numerical solution.

Table 5 presents the results for the GCI values in percent. These values determined the convergence rate of the numerical solution as compared to the grid resolution. The GCI asymptotic was equal to 0.95, indicating that the resolutions Re_3, Re_5, and Re_6 reached a grid-independent solution. The apparent order achieved in the simulation p is large due to a small grid refinement ratio of 1.1. The GCI percentage values for Re_5 and Re_6 are below the asymptotic threshold of 0.947, which implies convergence toward a grid-independent solution. The extrapolated value suggests that the solution obtained on the grid (Re_3) achieved an independent result.

TABLE 5 Grid convergence study over 3 grids. ϕ represents the value for the average velocity and $\phi_{extrapolated}$ its extrapolated value. N_{cells} is the number of grid elements, r the refinement ration between two successive grids. GCI is the grid convergence index in percent and its asymptotic value is provided by $GCI_{asymptotic}$, where a value close to unity indicates a grid independent solution. The order achieved in the simulation is given by p.

	ϕ	N_{cells}	r	GCI	$GCI_{asymptotic}$	p	$\phi_{extrapolated}$
Re_6	5.409e+00	7187500	1.1	4.26%			
Re_5	5.76e+00	5625000	1.2	4.73%	0.947	2.23	4.67e+00
Re_3	6.61e+00	3562500	-	-			

5 DISCUSSION

Grid independence studies for hydro-geomorphologic models applied to fluvial systems at both field and laboratory scales are essential for improving the performance of parallelized physics-based models, minimizing computational expense, maximizing model accuracy, and evaluating data representation across multiple computational domains. Fluvial models must consider how computational domain resolution affects simulated flow quantities, as simulations can vary with grid size (Lee et al. 2020; Samion et al. 2019; Roache 1998). This study addressed the gaps in grid convergence studies and their role in simulating turbulent flow in river systems at the field scale. To our knowledge, this research is one of the few grid independence studies

on CFD models for fluvial applications (some studies addressing this issue are Altenau et al. (2017), Yu and Lane (2011), and Lane et al. (1999)) and one of the first to apply grid independence to field-scale LES models in a river reach.

This study presented a novel approach to evaluate the impact of changes in spatial resolution on field-scale DES models to identify turbulent flow patterns in hydraulic features in canyon-bound rivers. The methodological framework incorporated seven different computational domain resolutions to analyze the sensitivity of field-scale models to spatial resolution changes by employing techniques such as TKE spectrum, spatiotemporal analysis of eddy structures, KL-divergence, NSE coefficient, wavelet power spectrum, GCI calculation. This study evaluated the loss of information and the data representation of anisotropic turbulence in a fine to coarse computational domain resolution set. The proposed metrics could evaluate the sensitivity of the field-scale model to the spatial resolution of the computational domain in the ability to identify complex turbulent flow patterns and hydraulic features in river systems, such as primary, secondary flows, vorticity patterns, and shear layers. The spatiotemporal distributed analysis clarifies the understanding of how domain resolution can affect the simulation results. Thus, this research work can contribute significantly to the computational modeling field in fluvial geomorphology, as the applications of eddy-resolving models are increasing to simulate field-scale river reaches. Overall, the proposed methodological framework can be employed to develop more efficient grid resolutions to simulate complex fluvial environments. Furthermore, this research can serve as a methodology for model transferability in other river-reach settings. Nonetheless, a validation process is necessary to assess the loss of information of an eddy-resolving model compared with a data collection.

The results suggest that the use of moment-based statistical metrics, such as mean and variance, is an optimal approach that minimizes information loss in DES models, compared to arbitrary techniques. Minimum divergence filtering algorithms are aimed at minimizing the KL-divergence and are based on entropy minimization. This finding has significant implications for minimum divergence filtering algorithms, which aimed to minimize KL-divergence instead of MSE. The medium and fine grid resolutions showed less information loss and a minimized divergence between the simulated and benchmark probability distributions. However, using a higher grid resolution also increased the computational cost of the simulation. The analysis derived from RMSE surfaces, KL-divergence, NSE coefficient, GCI approach, and flow structures suggested that the medium domain (Re_3) resolution is the minimum grid size required to obtain accurate simulation results in terms of capturing flow behavior and hydraulic characteristics, including secondary flows, return currents, shear layers, and primary and secondary flows. Below this threshold, the simulation results may be unreliable or significantly different from the benchmark case scenario results. Areas of the flow field were identified where the simulation is particularly sensitive to grid sizes, such as the separation and reattachment zones and the zones near the secondary eddy. These areas may require a larger grid resolution to capture the flow behavior accurately.

The increased computational cost of eddy-resolving models can make them impractical and unjustifiable for some applications, particularly those involving large spatial and temporal scales or long simulation times, scale order of days, or months. This grid independence study required multiple simulations at different grid resolutions. For instance, the finest grid resolution simulation required 85.6 hr of processing time on 120 processors to simulate 15 min in a 1-km river transect. Future work could focus on developing Machine Learning (ML) to enhance physics-based modeling (e.g., LES models) for domain geometry redefinition according to dominant physical processes. Overall, merging the PB and ML frameworks could contribute to optimizing the level of grid refinement in areas of interest, reducing the computational expenses of the simulation, and optimizing the grid refinement.

The findings of this study represent a significant advancement in our understanding of turbulent flow dynamics and sediment transport in large-scale river systems. By employing a physics-based modeling approach validated through field observations, this research has specifically focused on canyon-bound rivers, particularly in areas characterized by rapids and pools. Further investigation is necessary to assess the applicability of these findings to other river geometries that experience massive flow separation, such as sharp meander bends, river confluences, vegetated channels, or channels with hydraulic structures. These environments introduce different flow complexities, including secondary flows and localized turbulence, which may influence sediment transport and morphodynamic processes. The DES model used in this study has effectively captured macro-turbulence in the context of large-scale canyon-bound rivers. Still, its application to more diverse river settings requires further validation. Future research should aim to test the model in environments with varying bathymetric and hydraulic conditions, ensuring the

framework can accurately predict flow behavior across a broader range of river systems.

In the future, eddy-resolving models augmented with ML could introduce prior knowledge on the domain topology by coupling an adaptive mesh resolution algorithms module to the LES model to dynamically re-define the computational domain where the turbulent processes need to be represented and resolved, such as the lateral separation zones and main hydraulic features. ML can be used to learn complex relationships in simulations of eddy-resolving models, including augmentation of simulated data, identification of hidden patterns, and time series analysis. Furthermore, data compression ML algorithms can improve computational cost and data storage of objective simulated data analysis. Thus, data compression techniques, such as lossless and lossy compression, could potentially reduce the data size without compromising the simulated output results (Ju et al. 2022; Lagares and Araya 2013; Margetis et al. 2023). Post-processing techniques, such as data reduction and feature extraction, could be explored to extract objective information from the simulations.

6 CONCLUSIONS

The computational domain resolutions Re_3, Re_4, Re_5 and Re_6 successfully captured higher energy values at higher frequencies in the PSD than those captured by resolutions Re_0, Re_1, and Re_2; these results are relevant for examining frequencies that correspond to smaller-scale fluctuations with shorter wavelengths. The resolutions Re_6 and Re_4 captured smaller scales of turbulence and provided a more accurate representation of the TKE spectrum compared to the benchmark case scenario Re_5. The TKE spectrum exhibited a range of scales, from large-scale motions associated with the overall flow behavior to small-scale motions associated with highly localized turbulence for all the computational domain resolutions. Small-scale turbulence, such as that found in the viscous sublayer of a boundary layer, can experience significant TKE dissipation due to high turbulence levels, shear forces, and rapid fluctuations in velocity. Furthermore, it can affect the dynamics of turbulent eddies and the overall flow structure, especially in the near-wall region where TKE dissipation is most pronounced.

The wavelet spectrum of velocity successfully captured the ability of the six computational domain resolutions to represent eddy pulsation patterns at spatial-temporal scales to the benchmark case scenario. For domain resolutions Re_3, Re_4, and Re_6, the separation zone displayed a high-frequency eddy pulsation with a high amplitude. In contrast, lower-frequency eddy pulsations characterized the reattachment zone. Domain resolutions Re_0, Re_1, and Re_2 produced results that varied in frequency, period, and amplitude compared to the benchmark simulation Re_5. The power spectrum analysis for all domain resolutions identified three distinct regions with different spectral behaviors in the separation zone, primary, and secondary eddy. The first region exhibited a flat PSD across all frequencies below 0.001 Hz, indicating the presence of white noise in that frequency region. The second region, between 0.001 and 0.5 Hz, showed a Brownian walk behavior. The third region, with frequencies higher than 0.5 Hz, showed a flatter spectrum with a more uniform energy distribution at different frequencies. The non-stationary signals exhibited periodic and coherent signals of high amplitude and high frequency in the separation zone and low frequencies in the reattachment zone, as captured by the model. These signals were weaker in the near-surface grid cells compared to the signals observed at six-tenths of the channel depth grid cells. The resolution Re_5 captured the eddy pulsations in greater detail, representing more periodic and persistent signals between 4 and 2 min.

The RMSE values suggest that once the domain resolution Re_3 is reached, the RMSE values become relatively insensitive to further grid refinement. The RMSE surface analysis identified areas of the flow field that are particularly sensitive to grid sizes and may require a larger grid resolution to capture the flow behavior accurately. Minimum divergence filtering algorithms that aim to minimize KL-divergence instead of MSE were observed to minimize information loss. According to the KL and NSE results, Re_3 resolution was identified as a critical threshold or the minimum grid size required to obtain accurate simulation results to capture flow behavior and hydraulic characteristics, including secondary flows, return currents, shear layers, and primary and secondary eddies. The GCI quantitative analysis was used to estimate the numerical error due to discretization and determine the necessary grid resolution for achieving the desired level of accuracy. When using a fixed time step (0.1s), the extrapolated solution will inevitably contain a time discretization error.

In summary, the PSD of velocity fluctuations showed that resolutions Re_3, Re_4, Re_5, and Re_6 captured higher energy values at higher frequencies compared to Re_0, Re_1, and Re_2, indicating better resolution of smaller-scale fluctuations. The TKE spectrum for higher resolution domains (Re_4, Re_5, and Re_6) closely matched the benchmark case, unlike lower resolutions. RMSE values were lowest for Re_3, Re_4, and Re_6, becoming insensitive to further refinement beyond Re_3. KL-divergence values were lowest for Re_3 and Re_4, suggesting these resolutions reduce information loss and better approximate the benchmark. NSE

values stabilized for Re_3 and higher resolutions, indicating grid refinement beyond Re_3 did not significantly impact results. GCI values confirmed that Re_3, Re_5, and Re_6 achieved a grid-independent solution. Based on RMSE, KL-divergence, and GCI, the model showed predictive capabilities after reaching domain resolution Re_3.

Re_3 is recommended as the optimum grid, based on the statistical metrics PSD, RMSE, NSE, and GCI. This grid resolution could be transferred and applied to the study of other fan eddy complexes located along the Colorado River downstream of the Glen Canyon Dam with similar geomorphologic and bathymetric conditions and perhaps other similar canyon-bound rivers featured by rapids and pools.

References

Alexandrov, A., L. Dorodnicyn, Alexey Duben', and Dmitriy Kolyukhin (Feb. 2022). "Generation of Anisotropic Turbulent Velocity Fields Based on a Randomized Spectral Method". In: *Math. Models Comput. Simul.* 14, pp. 92–98. DOI: 10.1134/S2070048222010033.

Almohammadi, K. M., D. B. Ingham, L. Ma, and M. Pourkashan (Sept. 2013). "Computational fluid dynamics (CFD) mesh independency techniques for a straight blade vertical axis wind turbine". en. In: *J. Energy* 58, pp. 483–493. ISSN: 0360-5442. DOI: 10.1016/j.energy.2013.06.012.

Altenau, Elizabeth H., Tamlin M. Pavelsky, Paul D. Bates, and Jeffrey C. Neal (2017). "The effects of spatial resolution and dimensionality on modeling regional-scale hydraulics in a multichannel river". In: *Water Resour. Res.* 53.2, pp. 1683–1701. DOI: 10.1002/2016WR019396.

Alvarez, Laura V. (2015). *Turbulence, sediment transport, erosion, and sandbar beach failure processes in grand canyon*. PhD Thesis: Arizona State University.

Alvarez, Laura V. and Paul E. Grams (2021). "An Eddy-Resolving Numerical Model to Study Turbulent Flow, Sediment, and Bed Evolution Using Detached Eddy Simulation in a Lateral Separation Zone at the Field-Scale". In: *J. Geophys. Res. Earth Surf.* 126.10, e2021JF006149. DOI: 10.1029/2021JF006149.

Alvarez, Laura V., Mark W. Schmeeckle, and Paul. E. Grams (2017). "A detached eddy simulation model for the study of lateral separation zones along a large canyon-bound river". In: *J. Geophys. Res. Earth Surf.* 122.1, pp. 25–49. DOI: 10.1002/2016JF003895.

Alvarez, Laura. V. and Mark W. Schmeeckle (2013). "Erosion of river sandbars by diurnal stage fluctuations in the Colorado River in the Marble and Grand Canyons: full-scaled laboratory experiments". In: *River Res. Appli.* 29.7, pp. 839–854. ISSN: 1535-1467. DOI: 10.1002/rra.2576.

Aupoix, B. and P.R. Spalart (Aug. 2003). "Extensions of the Spalart–Allmaras turbulence model to account for wall roughness". en. In: *Int. J. Heat Fluid Flow* 24.4, pp. 454–462. ISSN: 0142727X. DOI: 10.1016/S0142-727X(03)00043-2.

Baker, Nazar, Ger Kelly, and Paul D. O'Sullivan (Oct. 2020a). "A grid convergence index study of mesh style effect on the accuracy of the numerical results for an indoor airflow profile". In: *Int. J. Vent.* 19.4, pp. 300–314. ISSN: 1473-3315. DOI: 10.1080/14733315.2019.1667558.

– (2020b). "A grid convergence index study of mesh style effect on the accuracy of the numerical results for an indoor airflow profile". In: *Int. J. Vent.* 19.4, pp. 300–314. DOI: 10.1080/14733315.2019.1667558.

Bhushan, S., M. Elmellouki, D.K. Walters, Y.A. Hassan, E. Merzari, and A. Obabko (2022). "Analysis of turbulent flow and thermal structures in low-Prandtl number buoyant flows using direct numerical simulations". In: *Int. J. Heat Mass Transf.* 189, p. 122733. ISSN: 0017-9310. DOI: 10.1016/j.ijheatmasstransfer.2022.122733.

Buscombe, D., P. E. Grams, and M. A. Kaplinski (2014). "Characterizing riverbed sediment using high-frequency acoustics: 2. Scattering signatures of Colorado River bed sediment in Marble and Grand Canyons". In: *J. Geophys. Res. Earth Surf* 119.12, pp. 2692–2710. DOI: 10.1002/2014JF003191.

Celik, Ismail B., Urmila Ghia, Patrick J. Roache, and Christopher J. Freitas (July 2008). "Procedure for Estimation and Reporting of Uncertainty Due to Discretization in CFD Applications". In: *J. Fluids Eng. Trans. ASME* 130.7. ISSN: 0098-2202. DOI: 10.1115/1.2960953.

Chaloner, Kathryn and Isabella Verdinelli (1995). "Bayesian Experimental Design: A Review". In: *Stat. Sci.* 10.3, pp. 273–304. DOI: 10.1214/ss/1177009939.

Chen, Goong, Qingang Xiong, Philip J Morris, Eric G Paterson, Alexey Sergeev, and Y Wang (2014). "OpenFOAM for computational fluid dynamics". In: *Notices of the AMS* 61.4, pp. 354–363. DOI: 10.1090/noti1095.

Chen, Kebing, Yifan Zhang, and Qiang Zhong (2019). "Wavelet coherency structure in open channel flow". In: *Water* 11.8, p. 1664. DOI: 10.3390/w11081664.

Coelho, P. J. and J. Argain (July 1997). "A local grid refinement technique based upon Richardson extrapolation". en. In: *Appl. Math. Model.* 21.7, pp. 427–436. ISSN: 0307-904X. DOI: 10.1016/S0307-904X(97)00037-1.

Converse, Yvette K, Charles P Hawkins, and Richard A Valdez (1998). "Habitat relationships of subadult humpback chub in the Colorado River through Grand Canyon: spatial variability and implications of flow regulation". en. In: *Regul. Rivers Res. Manage.* 14, p. 18.

Courant, Richard, Kurt Friedrichs, and Hans Lewy (1928). "Über die partiellen Differenzengleichungen der mathematischen Physik". In: *Math. Ann.* 100.1, pp. 32–74. DOI: 10.1007/BF01448839.

D'Ortenzio, Alessandro, Costanzo Manes, and Umut Orguner (2022). "A Model Selection criterion for the Mixture Reduction problem based on the Kullback - Leibler Divergence". In: *2022 25th International Conference on Information Fusion (FUSION)*, pp. 1–8. DOI: 10.23919/FUSION49751.2022.9841270.

Dodrill, M. J., C. B. Yackulic, B. Gerig, W. E. Pine, J. Korman, and C. Finch (Dec. 2015). "Do Management Actions to Restore Rare Habitat Benefit Native Fish Conservation? Distribution of Juvenile Native Fish Among Shoreline Habitats of the Colorado River: DISTRIBUTION OF JUVENILE NATIVE FISH, COLORADO RIVER". en. In: *River Res. Appl.* 31.10, pp. 1203–1217. ISSN: 15351459. DOI: 10.1002/rra.2842.

Draut, A and Rubin (2008). *The role of eolian sediment in the preservation of archeologic sites along the Colorado River corridor in Grand Canyon National Park, Arizona.* en. Professional Paper. Series: Professional Paper, p. 1756.

Durbin, P A and B. A. Pettersson Reif (June 2011). *Statistical Theory and Modeling for Turbulent Flows*. en. John Wiley & Sons. ISBN: 978-1-119-95752-2.

Eça, L. and M. Hoekstra (Apr. 2014). "A procedure for the estimation of the numerical uncertainty of CFD calculations based on grid refinement studies". en. In: *J. Comput. Phys.* 262, pp. 104–130. ISSN: 0021-9991. DOI: 10.1016/j.jcp.2014.01.006.

Ferziger, Joel H. (1985). "Large Eddy Simulation: Its Role in Turbulence Research". en. In: *Theoretical Approaches to Turbulence*. Ed. by D. L. Dwoyer, M. Y. Hussaini, and R. G. Voigt. Applied Mathematical Sciences. New York, NY: Springer, pp. 51–72. ISBN: 978-1-4612-1092-4. DOI: 10.1007/978-1-4612-1092-4_3.

Ferziger, Joel H. and Milovan Peric (2002). *Computational Methods for Fluid Dynamics*. en. 3rd ed. Berlin Heidelberg: Springer-Verlag. ISBN: 978-3-642-56026-2. DOI: 10.1007/978-3-642-56026-2.

Fiedler, H.E. (1988). "Coherent structures in turbulent flows". In: *Prog. Aerosp. Sci.* 25.3, pp. 231–269. ISSN: 0376-0421. DOI: 10.1016/0376-0421(88)90001-2.

Garcia, Marcelo, ed. (May 2008). *Sedimentation Engineering: Processes, Measurements, Modeling, and Practice*. en. Reston, VA: American Society of Civil Engineers. ISBN: 978-0-7844-0814-8 978-0-7844-7128-9. DOI: 10.1061/9780784408148.

Garrett, Van De Vanter, and Graf (1993). *United States Bureau of Reclamation and Geological Survey, streamflow and sediment-transport data, Colorado River and three tributaries in Grand Canyon, Arizona, 1983 and 1985-86,* en. Open-File Report. Series: Open-File Report. Tucson, Arizona: U.S. Geological Survey.

Gerig, Brandon, Michael J. Dodrill, and William E. Pine (Jan. 2014). "Habitat Selection and Movement of Adult Humpback Chub in the Colorado River in Grand Canyon, Arizona, during an Experimental Steady Flow Release". en. In: *N. Am. J. Fish. Manag.* 34.1, pp. 39–48. ISSN: 0275-5947, 1548-8675. DOI: 10.1080/02755947.2013.847880.

Grams, P. E (1997). "Geomorphology of the Green River in Dinosaur National Monument All Graduate Theses and Dissertations. 6703." en. In: p. 151. DOI: 10.26076/78e2-ae8c.

Grams, Paul. E., Laura V. Alvarez, M. Kaplinski, and S. Wright (2021). "Repeat measurements of bathymetry, streamflow velocity and sediment concentration made during a high flow experiment on the Colorado River in Grand Canyon, March 2008". In: *Geological Survey data release*. DOI: 10.5066/P9O00Z44.

Grinstein, Fernando F, Len G Margolin, and William J Rider (2007). *Implicit Large Eddy Simulation: Computing Turbulent Fluid Dynamics*. en. OCLC: 609840516. Leiden: Cambridge University Press. ISBN: 978-0-511-53974-9.

Gupta, Hoshin V., Harald Kling, Koray K. Yilmaz, and Guillermo F. Martinez (2009). "Decomposition of the mean squared error and NSE performance criteria: Implications for improving hydrological modelling". In: *J. Hydrol.* 377.1, pp. 80–91. ISSN: 0022-1694. DOI: 10.1016/j.jhydrol.2009.08.003.

Harpman, David A. (1999). "Assessing the Short-Run Economic Cost of Environmental Constraints on Hydropower Operations at Glen Canyon Dam". In: *Land Econ.* 75.3. Publisher: [Board of Regents of the University of Wisconsin System, University of Wisconsin Press], pp. 390–401. ISSN: 0023-7639. DOI: 10.2307/3147185.

Hartwell, Meredith A (2020). *U.S. Geological Survey Grand Canyon Monitoring and Research Center Fiscal Year 2020 Annual Project Report to the Glen Canyon Dam Adaptive Management Program*. en. Open-File Report. Flagstaff, Arizona: U.S. Geological Survey, p. 222.

Howard, Alan and Robert Dolan (1981). "Geomorphology of the Colorado River in the Grand Canyon". In: *J. Geol.* 89.3, pp. 269–298.

Huber HA Georgia SK, Finley SD (2023). "Systematic Bayesian posterior analysis guided by Kullback-Leibler divergence facilitates hypothesis formation". In: *J. Theor. Biol.* 558, p. 111341. ISSN: 0022-5193. DOI: 10.1016/j.jtbi.2022.111341.

Huck, Violaine, François Morency, and Héloıse Beaugendre (2019). "Grid study for Delayed Detached Eddy-Simulation's grid of a pre-stalled wing". In: *CASI Aero 2019-Canadian Aeronautics and Space Institute's AERO 2019 Conference*.

Im, Yong-Hoon, Kang Y. Huh, Shinnosuke Nishiki, and Tatsuya Hasegawa (2004). "Zone conditional assessment of flame-generated turbulence with DNS database of a turbulent premixed flame". In: *Combust. Flame* 137.4, pp. 478–488. ISSN: 0010-2180. DOI: 10.1016/j.combustflame.2004.03.006.

Joyce, James M. (2011). "Kullback-Leibler Divergence". In: *International Encyclopedia of Statistical Science*. Ed. by Miodrag Lovric. Berlin, Heidelberg: Springer Berlin Heidelberg, pp. 720–722. ISBN: 978-3-642-04898-2. DOI: 10.1007/978-3-642-04898-2_327.

Ju, Yi, Adalberto Perez, Stefano Markidis, Philipp Schlatter, and Erwin Laure (2022). "Understanding the Impact of Synchronous, Asynchronous, and Hybrid In-Situ Techniques in Computational Fluid Dynamics Applications". In: *2022 IEEE 18th International Conference on e-Science (e-Science)*, pp. 295–305. DOI: 10.1109/eScience55777.2022.00043.

Al-Jumaili, Safaa Kh and Saad Mulahasan (2023). "Tracking motion of thermal turbulent structures at the water surface in compound channel flows using block matching algorithm". In: *Ain Shams Eng. J.* 14.3, p. 101898. DOI: 10.1016/j.asej.2022.101898.

Khosronejad, Ali, Ajay B. Limaye, Zexia Zhang, Seokkoo Kang, Xiaolei Yang, and Fotis Sotiropoulos (2023). "On the Morphodynamics of a Wide Class of Large-Scale Meandering Rivers: Insights Gained by Coupling LES With Sediment-Dynamics". In: *Journal of Advances in Modeling Earth Systems* 15.3, e2022MS003257. DOI: 10.1029/2022MS003257.

Kolmogorov, Andrey Nikolaevich (1941). "The local structure of turbulence in incompressible viscous fluid for very large Reynolds number". In: *Dokl. Akad. Nauk. SSSR*. Vol. 30, pp. 301–303.

Korman, Josh, Stephen M. Wiele, and Margaret Torizzo (July 2004). "Modelling effects of discharge on habitat quality and dispersal of juvenile humpback chub(Gila cypha) in the Colorado River, Grand Canyon". en. In: *River Res. Appl.* 20.4, pp. 379–400. ISSN: 1535-1459, 1535-1467. DOI: 10.1002/rra.749.

Kuwata, Y. and Y. Kawaguchi (Mar. 2019). "Direct numerical simulation of turbulence over systematically varied irregular rough surfaces". en. In: *J. Fluid Mech.* 862. Publisher: Cambridge University Press, pp. 781–815. ISSN: 0022-1120, 1469-7645. DOI: 10.1017/jfm.2018.953.

Lagares, Christian J. and Guillermo Araya (2013). "Evaluating the Impact of Lossy Compression on a Direct Numerical Simulation of a Mach 2.5 Turbulent Boundary Layer". In: *AIAA SCITECH 2023 Forum*. DOI: 10.2514/6.2023-1684.

Lane, S.N., K.F. Bradbrook, K.S. Richards, P.A. Biron, and A.G. Roy (1999). "The application of computational fluid dynamics to natural river channels: three-dimensional versus two-dimensional approaches". In: *Geomorphology* 29.1, pp. 1–20. ISSN: 0169-555X. DOI: 10.1016/S0169-555X(99)00003-3.

Lee, Minhyung, Gwanyong Park, Changyoung Park, and Changmin Kim (Dec. 2020). "Improvement of Grid Independence Test for Computational Fluid Dynamics Model of Building Based on Grid Resolution". en. In: *Adv. Civ. Eng* 2020. Publisher: Hindawi, p. 11. ISSN: 1687-8086. DOI: 10.1155/2020/8827936.

Lee and Akio Yamamoto (1994). "Wavelet analysis: theory and applications". In: *Hewlett-Packard j.* 45, pp. 44–44.

Leopold, Luna Bergere (1969). *The rapids and the pools - Grand Canyon: Chapter D in The Colorado River region and John Wesley Powell (Professional Paper 669)*. USGS Numbered Series 669-D. Washington, D.C.: U.S. Government Printing Office, p. 131145. DOI: 10.3133/pp669D.

Ligrani, Phillip M. and Robert J. Moffat (Jan. 1986). "Structure of transitionally rough and fully rough turbulent boundary layers". en. In: *J. Fluid Mech.* 162.-1, p. 69. ISSN: 0022-1120, 1469-7645. DOI: 10.1017/S0022112086001933.

Lomeli, Luis, Abdon Iniguez, Prasanthi Tata, Nilamani Jena, Zhong-Ying Liu, Richard Etten, Arthur Lander, Babak Shahbaba, John Lowengrub, and Vladimir Minin (Jan. 2021). "Optimal experimental design for mathematical models of haematopoiesis". In: *J. R. Soc. Interface* 18, p. 20200729. DOI: 10.1098/rsif.2020.0729.

Margetis, Andreas-Stefanos I., Evangelos M. Papoutsis-Kiachagias, and Kyriakos C. Giannakoglou (2023). "Reducing memory requirements of unsteady adjoint by synergistically using check-pointing and compression". In: *Int. J. Numer. Methods Fluids* 95.1, pp. 23–43. DOI: 10.1002/fld.5136.

McCuen, Richard, Zachary Knight, and A. Cutter (Nov. 2006). "Evaluation of the Nash–Sutcliffe Efficiency Index". In: *J. Hydrol. Eng.* 11. DOI: 10.1061/(ASCE)1084-0699(2006)11:6(597).

Melis, Theodore S., Carl J. Walters, and Josh Korman (2015). "Surprise and Opportunity for Learning in Grand Canyon: the Glen Canyon Dam Adaptive Management Program". In: *Ecol. Soc.* 20.3. ISSN: 1708-3087. DOI: 10.5751/ES-07621-200322.

Moriasi, Daniel, Jeff Arnold, Michael Van Liew, Ron Bingner, R.D. Harmel, and Tamie Veith (May 2007). "Model Evaluation Guidelines for Systematic Quantification of Accuracy in Watershed Simulations". In: *Trans. ASABE* 50. DOI: 10.13031/2013.23153.

Nagata, Nobuhisa, Takashi Hosoda, Tatsuaki Nakato, and Yoshio Muramoto (Dec. 2005). "Three-Dimensional Numerical Model for Flow and Bed Deformation around River Hydraulic Structures". en. In: *J Hydraul Eng* 131.12, pp. 1074–1087. ISSN: 0733-9429, 1943-7900. DOI: 10.1061/(ASCE)0733-9429(2005)131:12(1074).

Nash, J.E. and J.V. Sutcliffe (1970). "River flow forecasting through conceptual models part I — A discussion of principles". In: *J. Hydrol* 10.3, pp. 282–290. ISSN: 0022-1694. DOI: 10.1016/0022-1694(70)90255-6.

Navah, Farshad, Marta de la Llave Plata, and Vincent Couaillier (May 2020). "A high-order multiscale approach to turbulence for compact nodal schemes". en. In: *Comput. Methods Appl. Mech. Eng.* 363, p. 112885. ISSN: 0045-7825. DOI: 10.1016/j.cma.2020.112885.

Nearing, Grey S. and Hoshin V. Gupta (Jan. 2015). "The quantity and quality of information in hydrologic models". en. In: *Water Resour. Res.* 51.1, pp. 524–538. ISSN: 00431397. DOI: 10.1002/2014WR015895.

Nikora, Vladimir, Ian McEwan, Stephen McLean, Stephen Coleman, Dubravka Pokrajac, and Roy Walters (Aug. 2007). "Double-Averaging Concept for Rough-Bed Open-Channel and Overland Flows: Theoretical Background". en. In: *J Hydraul Eng* 133.8, pp. 873–883. ISSN: 0733-9429, 1943-7900. DOI: 10.1061/(ASCE)0733-9429(2007)133:8(873).

Noto, Katsuhisa (2009). "Direct Numerical Simulation of Isothermal Wake: DNS Noise, Strong Anisotropy Turbulence, and Vortex Dislocation Generation Mechanism". In: *Numer. Heat Transf. B: Fundam.* 56.2, pp. 167–189. DOI: 10 . 1080 / 10407790903116402.

Onofre R. Song Zhao, Zakaria Bouali and Arnaud Mura (2022). "DNS analysis of turbulent vaporizing two-phase flows, Part I: Topology of the velocity field". In: *Int. J. Multiph. Flow* 156, p. 104208. ISSN: 0301-9322. DOI: 10.1016/j.ijmultiphaseflow.2022.104208.

Özyilmaz, N., K. N. Beronov, and A. Delgado (2008). "Characterization of the Reynolds-stress and dissipation-rate decay and anisotropy from DNS of grid-generated turbulence". In: *PAMM* 8.1, pp. 10585–10586. DOI: 10.1002/pamm.200810585.

Patel, Saahil, Benjamin Collis, William Duong, Daniel Koch, Massimiliano Cutugno, Laura Wessing, and Paul Alsing (Mar. 2023). "Information loss and run time from practical application of quantum data compression". In: *Phys. Scr.* 98.4, p. 045111. DOI: 10.1088/1402-4896/acc492.

Phillips, Tyrone S. and Christopher J. Roy (Sept. 2014). "Richardson Extrapolation-Based Discretization Uncertainty Estimation for Computational Fluid Dynamics". In: *J. Fluids Eng.* 136.12. ISSN: 0098-2202. DOI: 10.1115/1.4027353.

Piasecka, Magdalena, Artur Piasecki, and Norbert Dadas (2022). "Experimental Study and CFD Modeling of Fluid Flow and Heat Transfer Characteristics in a Mini-Channel Heat Sink Using Simcenter STAR-CCM+ Software". In: *Energies* 15.2. DOI: 10.3390/en15020536.

Pope, S. B (Aug. 2000). *Turbulent Flows*. en. Cambridge University Press. ISBN: 978-0-521-59886-6.

Rees, Eric van (2014). "ArcGIS Pro 2D and 3D GIS". In: *GeoInformatics* 17.7, p. 38.

Roache, P. J. (Sept. 1994). "Perspective: A Method for Uniform Reporting of Grid Refinement Studies". In: *J. Fluids Eng.* 116.3, pp. 405–413. ISSN: 0098-2202. DOI: 10.1115/1.2910291.

– (1997). "Quantification of Uncertainty in Computational Fluid Dynamics". In: *Annu Rev Fluid Mech* 29.1, pp. 123–160. DOI: 10.1146/annurev.fluid.29.1.123.

Roache, Patrick J (1998). *Verification and validation in computational science and engineering*. eng. Vol. 895. Albuquerque, NM: Hermosa Albuquerque, NM. ISBN: 978-0-913478-08-0.

Roache, Patrick J. and Patrick M. Knupp (1993). "Completed Richardson extrapolation". en. In: *Commun Numer Methods Eng.* 9.5, pp. 365–374. ISSN: 1099-0887. DOI: 10.1002/cnm.1640090502.

Roy, Christopher J. (May 2005). "Review of code and solution verification procedures for computational simulation". en. In: *J. Comput. Phys.* 205.1, pp. 131–156. ISSN: 00219991. DOI: 10.1016/j.jcp.2004.10.036.

Rubin, D. M., D. Buscombe, S. A. Wright, D. J. Topping, P. E. Grams, J. C. Schmidt, J. E. Hazel Jr., M. A. Kaplinski, and R. Tusso (2020). "Causes of Variability in Suspended-Sand Concentration Evaluated Using Measurements in the Colorado River in Grand Canyon". In: *J. Geophys. Res. Earth Surf.* 125.9, e2019JF005226. DOI: 10.1029/2019JF005226.

Rubin, D. M. and R. R. McDonald (June 1995). "Nonperiodic Eddy Pulsations". en. In: *Water Resour. Res.* 31.6, pp. 1595–1605. ISSN: 00431397. DOI: 10.1029/95WR00472.

Ryan, Elizabeth G., Christopher C. Drovandi, James M. McGree, and Anthony N. Pettitt (2016). "A Review of Modern Computational Algorithms for Bayesian Optimal Design". In: *Int. Stat. Rev.* 84.1, pp. 128–154. DOI: 10.1111/insr.12107.

Safarzadeh, Akbar and Wernher Brevis (Mar. 2016). "Assessment of 3D-RANS models for the simulation of topographically forced shallow flows". en. In: *J. Hydrol. Hydromech.* 64.1, pp. 83–90. ISSN: 0042-790X. DOI: 10.1515/johh-2016-0008.

Samion, Siti Ruhliah Lizarose, Nur Haziqah Shaharuddin, and Mohamed Sukri Mat Ali (Mar. 2019). "Grid Convergence Study for Detached-Eddy Simulation of Flow over Rod-Airfoil Configuration Using OpenFOAM". en. In: *IOP Conf. Ser. Mater Sci. Eng.* 491. Publisher: IOP Publishing, p. 012023. ISSN: 1757-899X. DOI: 10.1088/1757-899X/491/1/012023.

Schmidt, John C. (Sept. 1990). "Recirculating Flow and Sedimentation in the Colorado River in Grand Canyon, Arizona". en. In: *J. Geol.* 98.5, pp. 709–724. ISSN: 0022-1376, 1537-5269. DOI: 10.1086/629435.

Schmidt, John C., P. E. Grams, and Michael F. Leschin (1999). "Variation in the Magnitude and Style of Deposition and Erosion in Three Long (8–12 Km) Reaches as Determined by Photographic Analysis". In: *The Controlled Flood in Grand Canyon*. American Geophysical Union (AGU), pp. 185–203. ISBN: 978-1-118-66471-1. DOI: 10.1029/GM110p0185.

Schmidt, John C. and David M. Rubin (1995). "Regulated streamflow, fine-grained deposits, and effective discharge in canyons with abundant debris fans". en. In: *Geophysical Monograph Series*. Ed. by John E. Costa, Andrew J. Miller, Kenneth W. Potter, and Peter R. Wilcock. Vol. 89. Washington, D. C.: American Geophysical Union, pp. 177–195. ISBN: 978-0-87590-046-9. DOI: 10.1029/GM089p0177.

Seifollahi Moghadam, Zahra, François Guibault, and André Garon (Jan. 2021). "On the Evaluation of Mesh Resolution for Large-Eddy Simulation of Internal Flows Using Openfoam". en. In: *Fluids* 6.1, p. 24. ISSN: 2311-5521. DOI: 10.3390/fluids6010024.

Shur, M, PR Spalart, M Strelets, and A Travin (1999). "Detached-eddy simulation of an airfoil at high angle of attack". In: *Engineering turbulence modelling and experiments 4*. Elsevier, pp. 669–678.

Sinha, Sanjiv K., Fotis Sotiropoulos, and A. Jacob Odgaard (Jan. 1998). "Three-Dimensional Numerical Model for Flow through Natural Rivers". en. In: *J Hydraul Eng* 124.1, pp. 13–24. ISSN: 0733-9429, 1943-7900. DOI: 10.1061/(ASCE)0733-9429(1998)124:1(13).

Smith, Aaron, Prasad A. Naik, and Chih-Ling Tsai (2006). "Markov-switching model selection using Kullback–Leibler divergence". In: *J. Econom.* 134.2, pp. 553–577. ISSN: 0304-4076. DOI: 10.1016/j.jeconom.2005.07.005.

Spalart, Philippe R (2009). "Detached-Eddy simulation". In: *Annual review of fluid mechanics* 41.1, pp. 181–202. DOI: 10.1146/annurev.fluid.010908.165130.

Spalart, Philippe R., William H. Jou, Mikhail Strelets, and Steven R. Allmaras (1997). "Comments on the Feasibility of LES for Wings and on the Hybrid RANS/LES Approach". In: *Proceedings of the First AFOSR International Conference on DNS/LES, 1997*, pp. 137–147.

Squires, Kyle D. (2004a). "Detached-Eddy Simulation: Current Status and Perspectives". en. In: *Direct and Large-Eddy Simulation V*. Ed. by Rainer Friedrich, Bernard J. Geurts, and Olivier Métais. ERCOFTAC Series. Dordrecht: Springer Netherlands, pp. 465–480. ISBN: 978-1-4020-2313-2. DOI: 10.1007/978-1-4020-2313-2_49.

– (2004b). "Detached-Eddy Simulation: Current Status and Perspectives". en. In: *Direct and Large-Eddy Simulation V*. Ed. by R. V. A. Oliemans, W. Rodi, Rainer Friedrich, Bernard J. Geurts, and Olivier Métais. Vol. 9. Series Title: ERCOFTAC Series. Dordrecht: Springer Netherlands, pp. 465–480. ISBN: 978-90-481-6575-9 978-1-4020-2313-2. DOI: 10.1007/978-1-4020-2313-2_49.

Torrence, Christopher and Gilbert P. Compo (1998). "A Practical Guide to Wavelet Analysis". In: *Bull. Am. Meteorol. Soc.* 79.1, pp. 61–78. DOI: 10.1175/1520-0477(1998)079<0061:APGTWA>2.0.CO;2.

Travin, Andrei, Michael Shur, Michael Strelets, and Philippe Spalart (2000). "Detached-eddy simulations past a circular cylinder". In: *Flow, turbulence and combustion* 63.1, pp. 293–313. DOI: 10.1023/A:1015779325146.

Turner, Benjamin L., Hector M. Menendez, Roger Gates, Luis O. Tedeschi, and Alberto S. Atzori (Dec. 2016). "System Dynamics Modeling for Agricultural and Natural Resource Management Issues: Review of Some Past Cases and Forecasting Future Roles". en. In: *Resources* 5.4. Number: 4 Publisher: Multidisciplinary Digital Publishing Institute, p. 40. DOI: 10.3390/resources5040040.

Van Hoecke, Laurens, Dieter Boeye, Arturo Gonzalez-Quiroga, Gregory S. Patience, and Patrice Perreault (2023). "Experimental methods in chemical engineering: Computational fluid dynamics/finite volume method—CFD/FVM". In: *Can. J. Chem. Eng.* 101.2, pp. 545–561. DOI: 10.1002/cjce.24571.

Wang, Yongqiang, Peng Zhang, Shengfa Yang, Chunhong Hu, Jianling Jin, and Rangang Zhang (2023). "Characteristics of Large-Scale Coherent Structures on Irregularly Arranged Rough-Bed Open-Channel Flows". In: *Water* 15.6. ISSN: 2073-4441. DOI: 10.3390/w15061105.

Webb, R. H., D. L. Wegner, E. D. Andrews, R. A. Valdez, and D. T. Patten (1999). "Downstream effects of Glen Canyon Dam on the Colorado River in Grand Canyon: A review". en. In: *Geophysical Monograph Series*. Ed. by Robert H. Webb, John C.

Schmidt, G. Richard Marzolf, and Richard A. Valdez. Vol. 110. Washington, D. C.: American Geophysical Union, pp. 1–21. ISBN: 978-0-87590-093-3. DOI: 10.1029/GM110p0001.

Wright, Scott A. and Matt Kaplinski (Mar. 2011). "Flow structures and sandbar dynamics in a canyon river during a controlled flood, Colorado River, Arizona: FLOW STRUCTURES AND SANDBAR DYNAMICS". en. In: *J. Geophys. Res. Earth Surf.* 116.F1, n/a–n/a. ISSN: 01480227. DOI: 10.1029/2009JF001442.

Xiao, Maochao, Yufei Zhang, and Haixin Chen (2017). "Numerical Study of an Iced Airfoil Using Window-Embedded RANS/LES Hybrid Method". In: *9th AIAA Atmospheric and Space Environments Conference*. American Institute of Aeronautics and Astronautics. DOI: 10.2514/6.2017-3761.

Yu, D. and S. N. Lane (2011). "Interactions between subgrid-scale resolution, feature representation and grid-scale resolution in flood inundation modelling". In: *Hydrological Processes* 25.1, pp. 36–53. DOI: 10.1002/hyp.7813.

Zaynetdinov, Konstantin, Srujal Shah, Mehran Kiani-Oshtorjani, and Payman Jalali (2023). "Direct numerical simulations for assessment of gas-solid drag models in two-dimensional random arrays of particles". In: *Adv. Powder Technol.* 34.1, p. 103880. ISSN: 0921-8831. DOI: 10.1016/j.apt.2022.103880.

Zhao, Chenchen and Hongyi Xu (2023). "Direct Numerical Simulations of Tandem Wings at Low Reynolds Number". In: *AIAA SCITECH 2023 Forum*. DOI: 10.2514/6.2023-1009.

Appendix

A Grid independence study using time series analysis

A.1 Energy spectrum

The energy cascade is described as the transfer of energy from low wavenumbers to high wavenumbers. This transfer brings turbulent kinetic energy (TKE) from large to small scales. The small-scale eddies affected by viscous forces are within the dissipation range of the scales; here, the turbulent energy is dissipated as heat (Figure A1). In the intermediate range of scales, the so-called inertial subrange, Kolmogorov's hypotheses led to the following universal form for the energy spectrum (Kolmogorov 1941): $E(k_1) = C\varepsilon^{2/3}k^{-5/3}$, where the energy spectrum of turbulence, $E(k)$, is related to the mean turbulence kinetic energy per unit mass, ε is the rate of turbulence kinetic energy dissipation, k is the wavenumber, and C is a Kolmogorov constant. In the inertial subrange, the rate at which turbulent energy is transferred to smaller scales depends only on the dissipation rate of turbulent energy. Eddy resolving models can only resolve the eddies above the grid cells, constraining the resolved energy cascade to the smallest eddies of the grid cell dimensions (Navah et al. 2020). The turbulent kinetic energy not resolved by the predetermined mesh must be taken into account in the subgrid scales. The Kolmogorov's turbulence spectrum equation $E(k_1) = C\varepsilon^{2/3}k^{-5/3}$ can be written as: $E(k_1) = \frac{1}{\Delta k_1}\frac{1}{N^2}\sum_{j=0}^{N/2-1}\hat{u}_j\hat{u}_j^*$, where N is the number of points probes that are transformed, $\hat{u}_j$ is the Fourier transform of u_1', $\hat{u}_j^*$ is the Fourier transform's complex conjugate, and Δk_1 is the spacing between points in the k_1 domain. This expression provides a representation of how the energy of a signal is distributed across different frequencies, and was used to determine the ability of the different grid resolutions to capture eddy pulsations and to evaluate the performance of the numerical models to capture turbulent structures of different scales (Wang et al. 2023; Al-Jumaili and Mulahasan 2023).

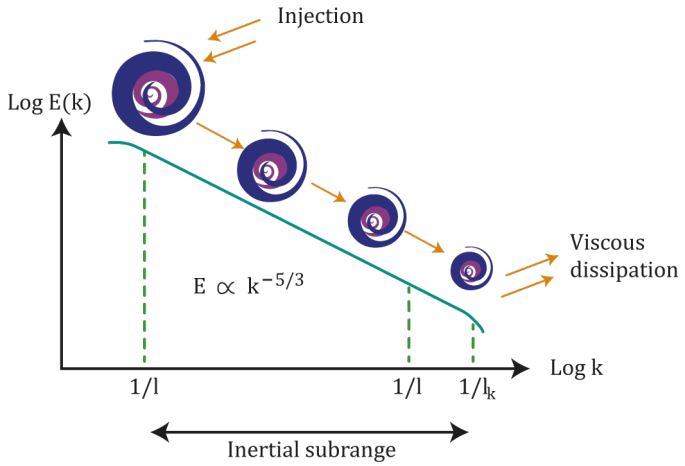

-25pt

FIGURE A1 Representation of the process of production, energy cascade, and dissipation in the energy spectrum of turbulence according to Kolmogorov's theory.

A.2 Wavelet spectrum:

The wavelet analysis technique involved adjusting the window of the short-time Fourier transform by either stretching or compressing it based on the desired frequency to be detected. This process helps to create scales in both the time and frequency domains, which is useful in identifying intermittent flow features such as coherent structures. Coherent structures refer to patterns or structures within a fluid flow that are dominant and recurring in time and space (Fiedler 1988). These structures are often responsible for the transfer of energy and momentum within the fluid and can significantly impact the flow behavior. Overall, wavelet analysis can be viewed as a method of identifying and locating specific frequencies that are of interest. (Chen et al.

2019). Wavelets are signal processing tools for investigating time-varying frequency spectrum characteristics of nonstationary signals. The study by Rubin and McDonald (1995) has shown that nonperiodic eddy pulsations occur along the studied reach of the EM fan-eddy complex, and turbulence is one of the main processes responsible for generating these eddy pulsations (Rubin and McDonald 1995; Rubin et al. 2020). The study also found that the intrinsic behavior of the eddy structures characterized non-periodic pulsations, as evidenced by time series measurements of the flow velocity and the position of the reattachment point (Rubin and McDonald 1995).

B Root Mean Square Error (RMSE) values

The objective of Appendix B is to present the percentages of the total area corresponding to different ranges of RMSE values for each computational domain resolution at six-tenths of the channel (averaged velocity of the vertical profile) and near-surface grids (maximum simulated velocity). Tables B1 and B2 provide additional support to the results discussed Subsection 4.3.1, Figures 15, 16, and 17, specifically about RMSE statistical values.

TABLE B1 Percentages of the total area corresponding to each range of RMSE values for each generated computational domain resolutions Re_0, Re_1, Re_2, Re_3, Re_4, and Re_6 at six - tenths of the channel depth grid cells.

Six - tenths of the channel depth grid cells						
RMSE (m/s)	Re_0	Re_1	Re_2	Re_3	Re_4	Re_6
0.04 - 0.24	1.36	4.95	8.30	0.02	23.63	18.26
0.25 - 0.34	7.10	10.09	10.36	18.49	26.60	24.67
0.35 - 0.44	7.22	16.50	14.54	27.53	9.89	17.61
0.45 - 0.64	32.83	39.24	40.85	15.59	29.34	26.04
0.65 - 0.84	33.23	15.09	13.00	26.47	9.89	12.10
0.85 - 1.2	7.52	4.55	3.81	10.79	0.65	1.19
1.3 - 2	6.65	6.38	5.79	1.11	0.00	0.13
2.1 - 3.8	4.08	3.21	3.35	0.00	0.00	0.00

TABLE B2 Percentages of the total area corresponding to each range of RMSE values for each generated computational domain resolutions Re_0, Re_1, Re_2, Re_3, Re_4, and Re_6 at the near-surface grid cells.

Near-surface grid cells						
RMSE	Re_0	Re_1	Re_2	Re_3	Re_4	Re_6
0.04 - 0.24	0.38	2.25	3.95	0.00	17.48	13.20
0.25 - 0.34	2.91	7.04	8.74	14.00	33.16	28.06
0.35 - 0.44	8.76	13.63	11.41	35.62	12.86	20.07
0.45 - 0.64	40.67	41.13	37.90	13.85	17.58	20.36
0.65 - 0.84	25.31	17.70	21.87	15.66	17.32	15.64
0.85 - 1.2	7.97	6.60	5.23	17.51	1.57	2.36
1.3 - 2	8.32	7.24	6.48	3.29	0.02	0.31
2.1 - 3.8	5.68	4.42	4.42	0.06	0.00	0.00

C Results of Probability Density Functions (PDFs) at each domain resolution

Appendix C displays the values of the moments of PDFs for the KL-divergence across all simulated computational domain resolutions. Table C3 is supplementary information to the findings discussed in Subsection 4.3.2, specifically complementing Figures 19 and 20.

TABLE C3 Moments of Probability density functions (PDFs) values of the Kullback-Leibler for all simulated computational domain resolutions.

Domain resolution	Min	1st Quantile	Median	Mean	Standard Deviation	Variance	3rd Quantile	Max
Re_0	0.000	0.003	0.041	0.101	0.186	0.035	0.061	0.647
Re_1	0.000	0.088	0.197	0.227	0.171	0.029	0.379	0.469
Re_2	0.000	0.146	0.177	0.242	0.171	0.029	0.381	0.469
Re_3	0.000	0.028	0.115	0.149	0.137	0.019	0.282	0.432
Re_4	0.000	0.035	0.104	0.148	0.143	0.020	0.274	0.462
Re_5	0.000	0.035	0.120	0.153	0.141	0.020	0.061	0.462
Re_6	0.000	0.020	0.095	0.150	0.143	0.020	0.197	0.476

D Simulated videos from the DES model

Appendix D presents animated movies that correspond to the simulated videos derived from the post-processing data of the DES model. The videos were created using the ParaFOAM tool, an open-source, multi-platform application designed for data analysis and visualization. These animated videos have been developed to illustrate the processes of turbulent flow and vortex structures. Specifically, they provide a comparison between the coarse grid resolution and the current grid, showcasing near-bed and surface velocity vectors, as well as elucidating large-scale vorticity structures in both the vertical and horizontal dimensions. A detailed analysis of these videos can be found in the manuscript in subsections 4.1 (velocity and vorticity patterns). The captions associated with the videos are presented in this appendix. The videos have been uploaded as separate AVI files.

Movie 1. Simulated video of velocity vectors at near-surface grid cells for the domain resolutions A) Re_0 (lowest resolution), B) Re_3 (medium resolution), C) Re_6 (finest resolution), and D) Re_5 (Benchmark case), based on the simulated averaged velocity (m/s). The length of mean surface velocity vectors ranges from 0 to 4.5 m/s.

Movie 2. Simulated video of the velocity field at near-surface grid cells for the domain resolutions A) Re_0 (lowest resolution), B) Re_3 (medium resolution), C) Re_6 (finest resolution), and D) Re_5 (Benchmark case), based on the simulated averaged velocity (m/s).

Movie 3. Simulated video of iso-surfaces of Q-criterion colored by velocity magnitude for the domain resolutions A) Re_0 (lowest resolution), B) Re_3 (medium resolution), C) Re_6 (finest resolution), and D) Re_5 (Benchmark case).

Movie 4. Simulated video of the vertical component of vorticity for the domain resolutions A) Re_0 (lowest resolution), B) Re_3 (medium resolution), C) Re_6 (finest resolution), and D) Re_5 (Benchmark case).